Universität Stuttgart

INSTITUT FÜR MECHANIK

Wave Based Structural Health Monitoring of Strands of Wires using Piezoelectric Transducers

Sudharsana Raamanujan Raman

Master Thesis

Guided by
Dipl.-Ing. Helge Sprenger
Prof. Dr.-Ing. habil. L.Gaul

Institut für Angewandte und Experimentelle Mechanik
Universität Stuttgart
o. Prof. Dr.-Ing. habil. L. Gaul
Prof. Dr.-Ing. A. Kistner

June 2010

Contents

1 Introduction

Electricity is considered to the driving force from the start of the 20th Century. With increase in average energy consumption and decrease in sources of energy it becomes inevitable to reduce the losses in energy transmission. The electrical energy is practically transmitted over long distances using strands of wires. These wires are continuously subjected to climate changes. These allow the wires to develop cracks in them and thereby increase the loss in transmission. Currently these high power lines are monitored for integrity by using helicopters that run through the length of the wire and check for cracks. This is a costly method.

1.1 Motivation

The motivation behind my thesis is to reduce the cost of maintenance and thereby reduce the transmission energy losses. This is achieved practically using piezoelectric transducers which send packets of waves, that travel long distances and can be used to detect the cracks based on reflections. Fig. 1.1 shows the comparison between the responses from a laser measurement for the same specimen with and without crack. The region shows the reflected components of the wave from the crack during wave propagation. The region B shows the reflected components from the cracks due to reflection of the wave at the end of the specimens. Thus we can clearly see a method can be obtained to predict the cracks present in the system.

1.2 Previous Work

Meitzler considered the propagation of elastic pulses in wires having a circular cross-section [14]. He attributed pulse distortion to the propagation of several modes. His experimental and theoretical results suggest that coupling between the various modes of propagation were responsible for the observed pulse distortion. Rizzo and Lanza di Scalea examined the wave propagation problem in seven-wire cables at the level of the individual wires [16]. Using wavelet transforms they identified the vibration

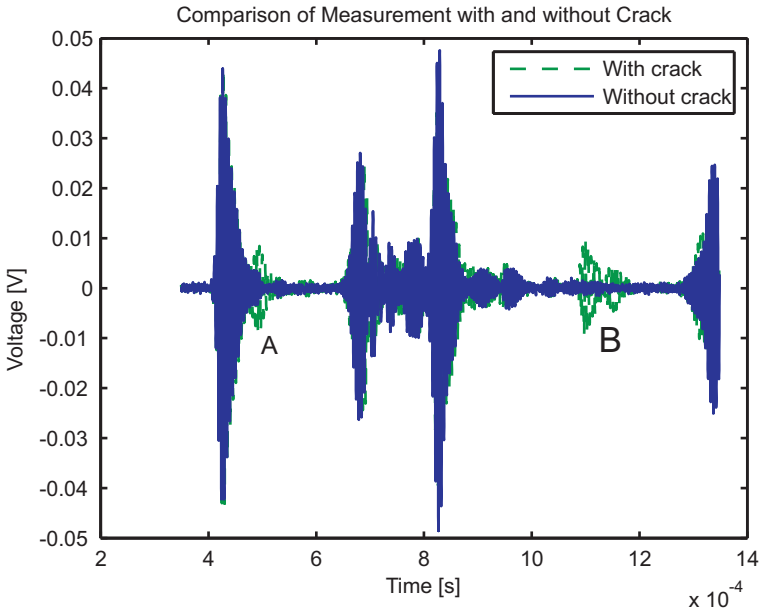

Figure 1.1: Comparison of Specimens with and without crack

modes which propagate with minimal losses. Such modes are really useful for long-range inspection of the wires. Furthermore, they found that since the dispersion curves are sensitive to the load level, the elastic waves could be used for continuous load monitoring. Haag, Beadle, Sprenger and Gaul proposed an energy model and a finite element model for modelling wave propagation [7]. They found out that the Finite element model requires more time compared to the energy based model but had the advantage of detecting the sub-surface defects. The main problem in the finite element method was the transducer ringing. Another problem that was identified when using the finite element model was the reflections occurring due to the presence of artificial boundaries.

1.3 Present Work

The goal of this master thesis is to clearly to make a finite element model of the wave propagation in the time domain. The first problem was to design the piezoelectric transducer in the finite element model and then use it for generating the waves and then find the suitable piezoelectric transducer for practical applications. During the finite element modelling, the reflections occurring in the artificial boundary was eliminated by using the non-reflecting boundary conditions or the absorbing boundary conditions. A new method for generating this boundary condition was also formu-

lated. The advantages of this new method being that it just used the finite element model as it is to predict the damping values for the wave absorption. This means that the user does not need to know the equations that govern the waves to find the values of the damping co-efficient. Thus this new method developed is not only useful for this current problem but can be extended to any problem where there is a wave propagation occurring with the only requirement being the knowledge of the cross-section in which the wave is propagating.

2 Fundamentals of Waves in Elastic Solids

2.1 The Wave Equation in Tensor Notations

In this section we can derive the wave equation in three dimensions from the basic principles [1]. Let $\mathbf{u}(\mathbf{x}, t)$ denote the displacement of particles. From the continuum theory, we can express deformation of the medium with the help of gradients of displacement vector. Assuming the linear theory, we end up with a linear small-strain tensor ϵ, with the components

$$\epsilon_{ij} = \frac{1}{2}(u_{i,j} + u_{j,i}) \tag{2.1}$$

It is also noted that the strain tensor is symmetric and hence $\epsilon_{ij} = \epsilon_{ji}$. According to the principle of balance of linear momentum, 'The instantaneous rate of change of the linear momentum of a body is equal to the resultant external forces acting on the body at the particular instant of time'. This can be described using the linearized theory as

$$\int_S \mathbf{t} dA + \int_V \rho \mathbf{f} dV = \int_V \rho \ddot{\mathbf{u}} dV \tag{2.2}$$

where $\mathbf{t}$ is the surface traction in the direction of the normal to the surface, $\mathbf{f}$ is the body force per unit mass, S is the surface that is subjected to the traction, V is the volume of the body and ρ is the density of the material. With the help of Cauchy Stress formula, we can have a relation between the stress tensor σ_{ji} and the traction forces as

$$t_i = \sigma_{ji} n_j \tag{2.3}$$

where σ_{ji} is the stress component in the x_i direction on the surface with unit normal n_j. By substituting the Eqn. 2.3 into Eqn. 2.2 we have in index notations

$$\int_S \sigma_{ji} n_j dA + \int_V \rho f_i dV = \int_V \rho \ddot{u}_i dV \tag{2.4}$$

By using Gauss theorem, we can transfer the surface integral into volume integral, hence rewriting Eqn. 2.4 we have

$$\int_V \sigma_{ji,j} + \rho f_i - \rho \ddot{u}_i dV = 0. \tag{2.5}$$

Since this is true for any part of V, we have

$$\sigma_{ji,j} + \rho f_i = \rho \ddot{u}_i \tag{2.6}$$

This is called as Cauchy's first law of motion.

The famous Hooke's law for relating the stresses and strains with the help Lame's Constant for a homogeneous, isotropic, linearly elastic body is given by

$$\sigma_{ji} = \lambda \epsilon_{kk} \delta_{ji} + 2\mu \epsilon_{ji} \tag{2.7}$$

Substituting the Hooke's law (Eqn. 2.7)and the strain tensor (Eqn. 2.1)in the Eqn. 2.6 we have the wave equation as below with changing the indices

$$\mu u_{i,jj} + (\lambda + \mu) u_{j,ji} + \rho f_i = \rho \ddot{u}_i \tag{2.8}$$

The Eqn. 2.8 represents the equation of motion of particles in an elastic continuum for an isotropic and homogeneous body. This forms our basis for further developments in this area.

2.2 Lamb Waves in Plates

Lamb waves have the property of travelling over long distances and can determine qualitatively and quantitatively the amount of damage occurring in the structure. These types of waves occur in plates. Here in this section, we can see about their history, the governing equations and try to visualize these waves using finite element method.

2.2.1 Mathematical Expression of Lamb Waves

The waves in a thin isotropic plate can be represented using a cartesian tensor notation in the form of

$$\mu \cdot u_{i,jj} + (\lambda + \mu) \cdot u_{i,ji} + \rho \cdot f_i = \rho \cdot \ddot{u}_i \tag{2.9}$$

where

u_i is the displacement in the x_i direction

f_i is the body force in the x_i direction

ρ is the density of the plate

μ is the shear modulus of the plate

$\lambda = \frac{2 \cdot \mu \cdot \nu}{1-2\nu}$ where λ is the Lamé constant and ν is the Poisson's Ratio

Based on Helmholtz decomposition, we can decompose Eqn. 2.9 into two uncoupled parts under the plane strain condition as

$$\begin{aligned} &\frac{\partial^2 \phi}{\partial x_1^2} + \frac{\partial^2 \phi}{\partial x_3^2} = \frac{1}{c_{\mathrm{L}}^2} \frac{\partial^2 \phi}{\partial t^2} \quad \text{is the governing equation for longitudinal modes and} \\ &\frac{\partial^2 \psi}{\partial x_1^2} + \frac{\partial^2 \psi}{\partial x_3^2} = \frac{1}{c_{\mathrm{T}}^2} \frac{\partial^2 \psi}{\partial t^2} \quad \text{is the governing equation for transverse modes} \end{aligned} \tag{2.10}$$

where

$$\phi = [A_1 \sin(p x_3) + A_2 \cos(p x_3)] \cdot \exp[i(k x_1 - \omega t)] \tag{2.11a}$$

$$\psi = [B_1 \sin(q x_3) + B_2 \cos(q x_3)] \cdot \exp[i(k x_1 - \omega t)] \tag{2.11b}$$

$$p^2 = \frac{\omega^2}{c_{\mathrm{L}}^2} - k^2, \quad q^2 = \frac{\omega^2}{c_{\mathrm{T}}^2} - k^2 \quad k = \frac{2\pi}{\lambda_{\mathrm{wave}}} \tag{2.11c}$$

A_1, A_2, B_1 and B_2 are four constants determined by the boundary condtions. k, ω and λ_{wave} are the wavenumber, circular frequency and wavelength of the wave

respectively. c_{L} and c_{T} are the velocities of longitudinal and transverse/shear modes defined by the following equations

$$c_{\mathrm{L}} = \sqrt{\frac{E(1-\nu)}{\rho(1+\nu)(1-2\nu)}} = \sqrt{\frac{2\mu(1-\nu)}{\rho(1-2\nu)}} \tag{2.12a}$$

$$c_{\mathrm{T}} = \sqrt{\frac{E}{2\rho(1+\nu)}} = \sqrt{\frac{\nu}{\rho}} \tag{2.12b}$$

where E is the Young's Modulus of the medium.

Lamb waves are actually superposition of longitudinal and transverse/shear modes. An infinte number of modes exist simultaneously, superimposing on each other between the upper and lower surface of the plate, finally leading to well behaved guided waves.

As a result of plane strain, the displacements in the wave propagation direction (x_1) and normal direction (x_3) can be described as

$$u_1 = \frac{\partial \phi}{\partial x_1} + \frac{\partial \psi}{\partial x_3} \quad u_2 = 0 \quad u_3 = \frac{\partial \phi}{\partial x_3} - \frac{\partial \psi}{\partial x_1} \tag{2.13}$$

From the displacement, we get the stresses as

$$\sigma_{31} = \mu(\frac{\partial u_3}{\partial x_1} + \frac{\partial u_1}{\partial x_3}) \quad = \mu(\frac{\partial^2 \phi}{\partial x_1 \partial x_3} - \frac{\partial^2 \psi}{\partial x_1^2} + \frac{\partial^2 \psi}{\partial x_3^2}) \tag{2.14a}$$

$$\sigma_{33} = \lambda(\frac{\partial u_1}{\partial x_1} + \frac{\partial u_3}{\partial x_3}) + 2\mu\frac{\partial u_3}{\partial x_3} = \lambda(\frac{\partial^2 \phi}{\partial x_1^2} + \frac{\partial^2 \phi}{\partial x_3^2}) + 2\mu(\frac{\partial^2 \phi}{\partial x_3^2} - \frac{\partial^2 \psi}{\partial x_1 \partial x_3}) \tag{2.14b}$$

For a plate with free upper and lower surfaces, by applying boundary conditions at both surfaces as follows

$$u(x,t) = u_0(x,t) \qquad \text{Displacement boundary condtion} \tag{2.15a}$$

$$t_i = \sigma_{ji} n_i \qquad \text{traction} \tag{2.15b}$$

$$\sigma_{31} = \sigma_{33} = 0 \quad at \quad x_3 = \pm d/2 = \pm h \tag{2.15c}$$

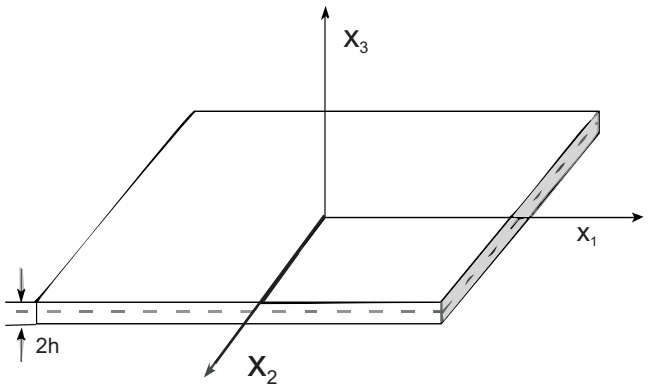

Figure 2.1: A plate with thickness = 2h

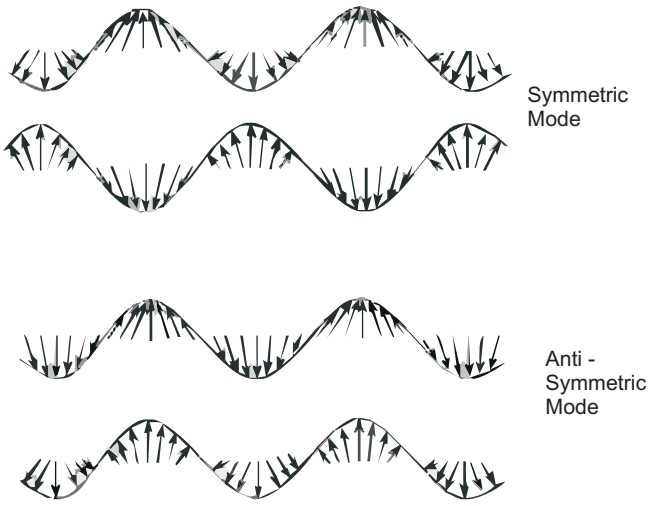

Figure 2.2: Symmetric and Antisymmetric Lamb Waves

where d is the plate thickness and h is the half thickness. For the plate coordinates see the Fig. 2.1

When we apply these boundary conditions to the Eqn. 2.13 and Eqn. 2.14, we obtain the description of Lamb waves in an isotropic and homogeneous plate as

$$\frac{\tan(qh)}{\tan(ph)} = \frac{4k^2qp\mu}{(\lambda k^2 + \lambda p^2 + 2\mu p^2)(k^2 - q^2)} \tag{2.16}$$

Substituting Eqn. 2.11c and Eqn. 2.12 into Eqn. 2.16 also taking into consideration that tan can be divided into since and cosine which have symmetric and antisymmetric properties, we can seperate Eqn. 2.16 into two parts as in a symmetric

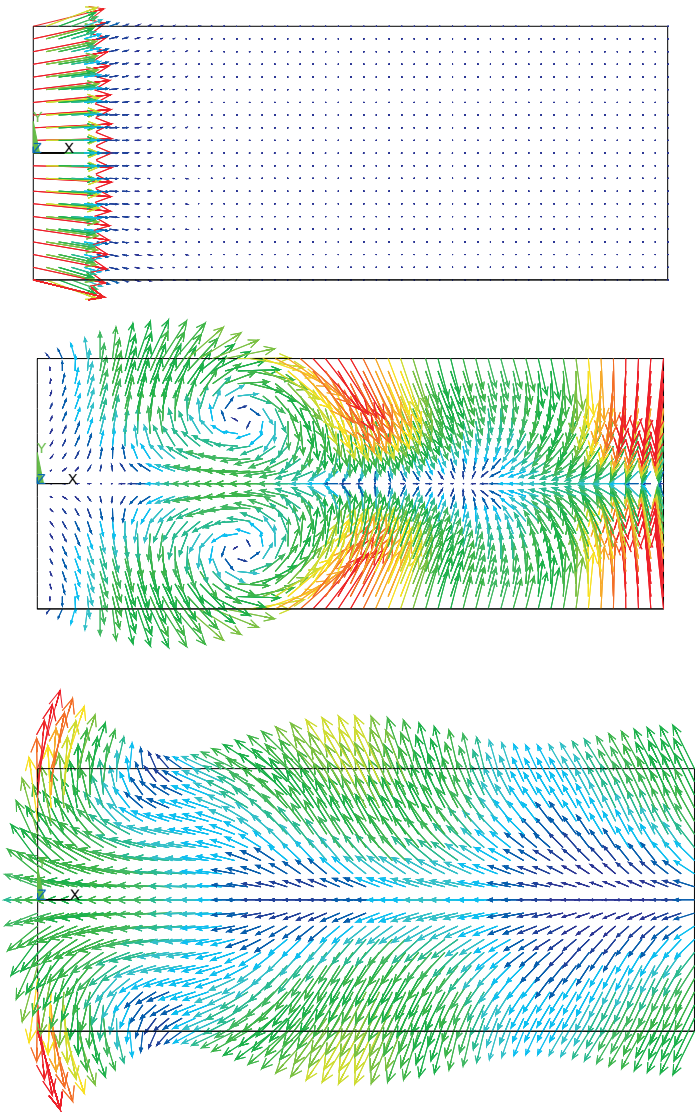

Figure 2.3: Finite element modelling of propagation of symmetric Lamb waves in a plate

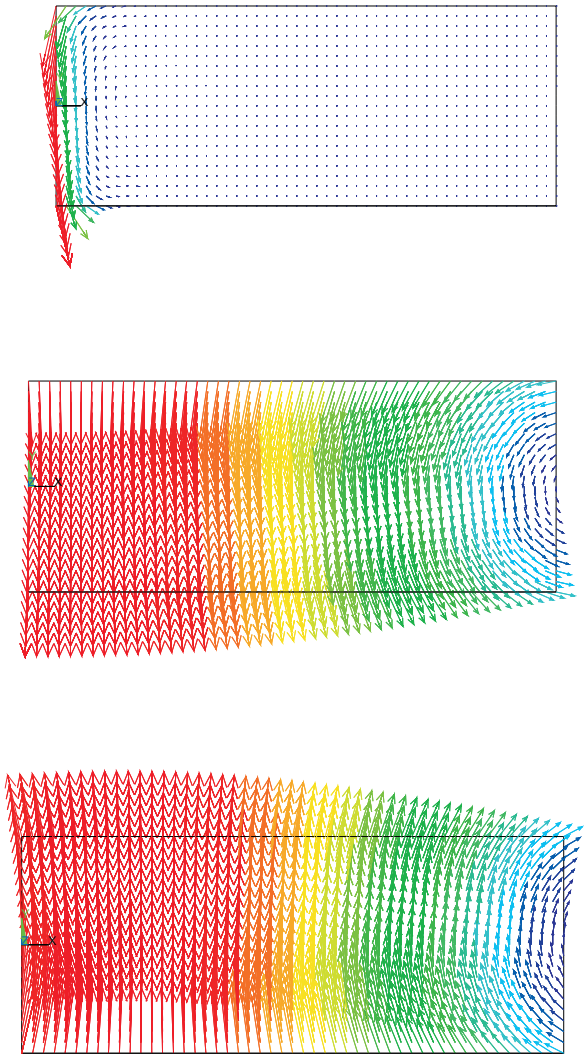

Figure 2.4: Finite element modelling of propagation of anti -symmetric Lamb waves in a plate

and antisymmetric part modes as

$$\frac{\tan(qh)}{\tan(ph)} = -\frac{4k^2qp}{(k^2-q^2)^2} \qquad \text{for symmetric modes} \tag{2.17a}$$

$$\frac{\tan(qh)}{\tan(ph)} = -\frac{(k^2-q^2)^2}{4k^2qp} \qquad \text{for anti-symmetric modes} \tag{2.17b}$$

2.2.2 Visualization of Lamb Waves

To view the Lamb waves, we used a frequency of 50 kHz. We created a time vector having 5 periods to act as the input. The displacement vector at each of the time point (10 points per period) was calculated using the equations and the input was given as a function boundary condition for the transient analysis. Eqn. 2.17 can be visualized to produce the symmetric and antisymmetric waves as shown in figure 2.2. The finite element modelling of generation of a lamb wave - the symmetric wave is modelled and is plotted with the help of vectors in Fig. 2.3. This plot is done using ANSYS. The antisymmetric lamb wave is plotted in Fig. 2.4. Comparing to the Fig. 2.2, we find that the symmetric and antisymmetric modes occur as expected in the finite element modelling. For the finite element modelling, the mesh sizes were controlled such that the mesh size of the length is 10 times smaller than the wavelength. Also absorbing boundary conditions were implemented with the help of a damping element. The modelling is detailed in the later chapters. Here the reader is just shown that lamb waves can be modelled with the help of finite elements.

2.3 Waves in Cylinders

This section deals with the various waves that are possible in a cylinder. These waves are similar to the Lamb waves in plates and have very high wave speeds. For example the longitudinal wave has a speed of 6300m/s in aluminium which suits our purpose perfectly.

2.3.1 Mathematical Basics

Here we can speak briefly about the mathematical basics behind the waves in cylinders. We use the cylindrical coordinates over the entire part of this section as it is easy to derive the wave equations. A solid, cylindrical rod in cylindrical coordinates is considered. The radius of the rod is a. The rod and coordinate system are shown

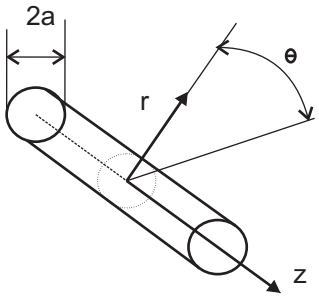

Figure 2.5: Rod with the Coordinate System

in Fig. 2.5.

The motion of any homogenous, isotropic, linear elastic body is governed by the so called Lamé - Navier-equation given by Eqn. 2.18

$$\mu\nabla^2\mathbf{u} + (\lambda+\mu)\nabla\nabla\cdot\mathbf{u} + \rho\mathbf{f} = \rho\ddot{\mathbf{u}} \tag{2.18}$$

By neglecting the body forces,we can decouple Equation 2.18 using Helmholtz decomposition we get Eqn. 2.19

$$\mathbf{u} = \nabla\phi + \nabla\times\psi \tag{2.19}$$

which can be written in scalar notations as

$$u_r = \frac{\partial\phi}{\partial r} + \frac{1}{r}\frac{\partial\psi_z}{\partial\theta} - \frac{\partial\psi_\theta}{\partial z} \tag{2.20}$$

$$u_\theta = \frac{1}{r}\frac{\partial\phi}{\partial\theta} + \frac{\partial\psi_r}{\partial z} - \frac{\partial\psi_z}{\partial r} \tag{2.21}$$

$$u_z = \frac{\partial\phi}{\partial z} + \frac{1}{r}\frac{\partial}{\partial r}(r\psi_\theta) - \frac{1}{r}\frac{\partial\psi_r}{\partial\theta} \tag{2.22}$$

With this substitution, the Lamé-Navier equation is decoupled into a scalar wave equation and a vector wave equation,

$$\nabla^2\phi = \frac{1}{c_{\mathrm{L}}^2}\frac{\partial^2\phi}{\partial t^2} \qquad \nabla^2\psi = \frac{1}{c_{\mathrm{T}}^2}\frac{\partial^2\psi}{\partial t^2} \tag{2.23}$$

This assumption for the displacements is complete and it covers all possible solutions

of Eqn. 2.18. The strains are given by the following equations

$$\varepsilon_{rr} = \frac{\partial u_r}{\partial r}, \qquad \varepsilon_{\theta\theta} = \frac{1}{r}\frac{\partial u_\theta}{\partial \theta} + \frac{u_r}{r} \tag{2.24a}$$

$$\varepsilon_{zz} = \frac{\partial u_z}{\partial z} \tag{2.24b}$$

$$\varepsilon_{r\theta} = \frac{1}{2}(\frac{1}{r}\frac{\partial u_r}{\partial \theta} + \frac{\partial u_\theta}{\partial r} - \frac{u_\theta}{r}) \tag{2.24c}$$

$$\varepsilon_{rz} = \frac{1}{2}(\frac{\partial u_z}{\partial r} + \frac{\partial u_r}{\partial z}) \tag{2.24d}$$

$$\varepsilon_{\theta z} = \frac{1}{2}(\frac{\partial u_\theta}{\partial z} + \frac{1}{r}\frac{\partial u_z}{\partial \theta}) \tag{2.24e}$$

Now by Hooke's Law we have

$$\sigma_{ij} = \lambda\Delta\delta_{ij} + 2\mu\varepsilon_{ij} \tag{2.25}$$

By using Eqn. 2.25 and Eqn. 2.24 we have the expression for the stresses given by the following equations

$$\sigma_{rr} = \lambda(\frac{\partial u_r}{\partial r} + \frac{u_r}{r} + \frac{1}{r}\frac{\partial u_\theta}{\partial \theta} + \frac{\partial u_z}{\partial z}) + 2\mu\frac{\partial u_r}{\partial r} \tag{2.26a}$$

$$\sigma_{\theta\theta} = \lambda(\frac{\partial u_r}{\partial r} + \frac{u_r}{r} + \frac{1}{r}\frac{\partial u_\theta}{\partial \theta} + \frac{\partial u_z}{\partial z}) + 2\mu(\frac{u_r}{r} + \frac{1}{r}\frac{\partial u_\theta}{\partial \theta}) \tag{2.26b}$$

$$\sigma_{zz} = \lambda(\frac{\partial u_r}{\partial r} + \frac{u_r}{r} + \frac{1}{r}\frac{\partial u_\theta}{\partial \theta} + \frac{\partial u_Z}{\partial z}) + 2\mu\frac{\partial u_z}{\partial z} \tag{2.26c}$$

$$\sigma_{r\theta} = \mu(\frac{\partial u_\theta}{\partial r} - \frac{u_\theta}{r} + \frac{1}{r}\frac{\partial u_r}{\partial \theta}) \tag{2.26d}$$

$$\sigma_{\theta z} = \mu(\frac{1}{r}\frac{\partial u_z}{\partial \theta} + \frac{\partial u_\theta}{\partial z}) \tag{2.26e}$$

$$\sigma_{zr} = \mu(\frac{\partial u_r}{\partial z} + \frac{\partial u_z}{\partial r}) \tag{2.26f}$$

For free surfaces, the stresses in the surface plane disappear, which also holds for the cylindrical surface of the investigated rod. The boundary conditions are thus described by Eqn. 2.27

$$\sigma_{rr} = \sigma_{r\theta} = \sigma_{rz} = 0 \qquad \text{here r=a} \tag{2.27}$$

In order to find a solution to the scalar and vector wave equations given by Eqn.2.23, the following general form is assumed for the scalar potential ϕ and the components of vector potential ψ as

$$\phi = f(r)\Theta_\phi(\theta)e^{i(\xi z-\omega t)} \tag{2.28a}$$

$$\psi_r = h_r(r)\Theta_r(\theta)e^{i(\xi z-\omega t)} \tag{2.28b}$$

$$\psi_\theta = h_\theta(r)\Theta_\theta(\theta)e^{i(\xi z-\omega t)} \tag{2.28c}$$

$$\psi_z = h_z(r)\Theta_z(\theta)e^{i(\xi z-\omega t)} \tag{2.28d}$$

The first two factors are independent of time. They describe the potential as a function of the location on a certain cross-section of the rod. An axial propagation of the potentials is achieved by the thrid factor. On substituting Eqn. 2.28a in the wave equation given by Eqn. 2.23 for ϕ we have

$$f''\Theta_\phi + \frac{1}{r}f'\Theta_\phi + \frac{1}{r^2}f\Theta_\phi'' - \xi^2 f\Theta_\phi = -\frac{\omega^2}{c_{\mathrm{L}}^2}f\Theta_\phi \tag{2.29}$$

Rearranging the terms, it leads to Eqn. 2.30

$$r^2\frac{f''}{f} + r\frac{f'}{f} - (\xi^2 - \frac{\omega^2}{c_{\mathrm{L}}^2})r^2 = -\frac{\Theta_\phi''}{\Theta_\phi} = n^2 \tag{2.30}$$

Since the solutions should be continuous functions, with continuous derivatives, n can only be zero or an integer. The two sides of Eqn. 2.30 containing the separated variables can only be equal to each other, if they are equal to the same constant. This constant is denoted by n^2. A solution of the Θ_ϕ of Eqn. 2.30 is

$$\Theta_\phi = A\sin n\theta + B\cos n\theta, n \in N \tag{2.31}$$

The same procedure yields similar expressions for Θ_r, Θ_θ and Θ_z.Considering only flexural, torsional and longitudinal modes, either sin- or cos- terms can be neglected. The general form of the potentials assumed in Eqn. 2.28 can be reduced to

$$\phi = f(r)\cos n\theta e^{i(\xi z-\omega t)} \tag{2.32a}$$

$$\psi_r = h_r(r)\sin n\theta e^{i(\xi z-\omega t)} \tag{2.32b}$$

$$\psi_\theta = h_\theta(r)\cos n\theta e^{i(\xi z-\omega t)} \tag{2.32c}$$

$$\psi_z = h_z(r)\sin n\theta e^{i(\xi z-\omega t)} \tag{2.32d}$$

The r dependence of the potentials is established from the Eqn. 2.30. Rearranging the same we have

$$\frac{d^2 f}{dr^2} + \frac{1}{r}\frac{df}{dr}(\alpha^2 - \frac{n^2}{r^2})f = 0 \tag{2.33}$$

where

$$\alpha^2 = \frac{\omega^2}{c_L^2} - \xi^2 \tag{2.34}$$

. Eqn. 2.33 is Bessel's Equation of order n. It is solved by

$$f(r) = AJ_n(\alpha r) \tag{2.35}$$

where J_n is a Bessel function of the first kind having order n. Solving for the remaining components is even more complicated, due to more complicated differential equations. The interested reader is referred to GRAFF [9]. The results are

$$h_z(r) = B_3 J_n(\beta r) \tag{2.36a}$$

$$h_r(r) = B_1 J_{n-1}(\beta r) + B_2 J_{n+1}(\beta r) \tag{2.36b}$$

$$h_\theta(r) = B_1 J_{n-1}(\beta r) - B_2 J_{n+1}(\beta r) \tag{2.36c}$$

with

$$\beta = \frac{\omega^2}{c_T^2} - \xi^2 \tag{2.37}$$

.

Inserting these results in the assumptions for displacements Eqn. 2.20 to Eqn. 2.22, we have

$$u_r = [f^{'} + \frac{n}{r}\psi_z + \xi\psi_r]\cos n\theta \exp^{i(\xi z - \omega t)} \tag{2.38a}$$

$$u_\theta = [-\frac{n}{r}f + \xi\psi_r - \psi_z^{'}]\sin n\theta \exp^{i(\xi z - \omega t)} \tag{2.38b}$$

$$u_z = [-\xi f^{'} - \psi_r^{'} - (n+1)\frac{\psi_r}{r}]\cos n\theta \exp^{i(\xi z - \omega t)} \tag{2.38c}$$

And accordingly the stresses in the surface become

$$\sigma_{rr} = [-\lambda(\alpha^2 + \xi^2)f + 2\mu(f^{''} + \frac{n}{r}(\psi_z^{'} - \frac{\psi_z}{r}) + \xi\psi_r^{'})]\cos n\theta e^{i(\xi z - \omega t)} \tag{2.39a}$$

$$\sigma_{r\theta} = \mu[\frac{2n}{r}(f^{'} - \frac{f}{r}) - (2\psi_z^{''} - \beta^2\psi_z) - \xi(\frac{n+1}{r}\psi_r - \psi_r^{'})]\sin n\theta e^{i(\xi z - \omega t)} \tag{2.39b}$$

$$\sigma_{rz} = \mu[-2\xi f^{'} - \frac{n}{r}(\psi_r^{'} + (\frac{n+1}{r} - \beta^2 + \xi^2)\psi_r) - \frac{n\xi}{r}\psi_z]\cos n\theta e^{i(\xi z - \omega t)} \tag{2.39c}$$

By using the boundary conditions as defined in the Eqn. 2.27, and substituting r=a leads to a general frequency equation given by

$$|a_{ij}| = 0 \tag{2.40}$$

where

$$a_{11} = \{\frac{\lambda(\alpha^2 + \xi^2)(\alpha a)^2}{2\mu\alpha^2} + (\alpha a)^2 - n^2\}J_n(\alpha a) + \alpha a J_n^{'}(\alpha a) \tag{2.41a}$$

$$a_{12} = \{n^2 - (\beta a)^2\}J_n(\beta a) - \beta a J_n^{'}(\beta a) \tag{2.41b}$$

$$a_{13} = 2n\{\beta a J_n^{'}(\beta a) - J_n(\beta a)\} \tag{2.41c}$$

$$a_{21} = n\{\alpha a J_n^{'}(\alpha a) - J_n(\alpha a)\} \tag{2.41d}$$

$$a_{22} = -n\{\beta a J_n^{'}(\beta a) = J_n(\beta a)\} \tag{2.41e}$$

$$a_{23} = -\{2n^2 - (\beta a)^2\} J_n(\beta a) + 2\beta a J_n^{'}(\beta a) \tag{2.41f}$$

$$a_{31} = -\alpha a J_n^{'}(\alpha a) \tag{2.41g}$$

$$a_{32} = -\frac{\beta^2 - \xi^2}{2\xi^2} \beta a J_n^{'}(\alpha a) \tag{2.41h}$$

$$a_{33} = n J_n(\beta a) \tag{2.41i}$$

This determinant specifies the frequency equation for all possible modes. To address particular mode families, n is varied. Thus we obtain the various modes and their frequencies of propagation in the cylindrical medium.

2.3.2 Longitudinal, Torsional and Flexural Modes in Cylinders

The waves that propagate in the cylinder are in one of these three types namely torsional, flexural and longitudinal. This part deals briefly the mathematics behind these modes and their wavefronts. This section uses the waveguide FE method [13] for generation of the wavefronts.

Longitudinal Waves

These types of waves are axially symmetric and have displacement components in the radial and axial directions. [1]. The first longitudinal mode is given by putting n=0 in the equation 2.41. The elements of the determinant become

$$a_{11}^{'} = \{\frac{\lambda(\alpha^2 + \xi^2)(\alpha a)^2}{2\mu\alpha^2} + (\alpha a)^2\} J_0(\alpha a) + \alpha a J_0^{'}(\alpha a) \tag{2.42a}$$

$$a_{12}^{'} = -(\beta a)^2 J_0(\beta a) - \beta a J_0^{'}(\beta a) \tag{2.42b}$$

$$a_{23}^{'} = (\beta a)^2 J_0(\beta a) + 2\beta a J_0^{'}(\beta a) \tag{2.42c}$$

$$a_{31}^{'} = -\alpha a J_0^{'}(\alpha a) \tag{2.42d}$$

$$a_{32}^{'} = -\frac{\beta^2 - \xi^2}{2\xi^2} \beta a J_0^{'}(\alpha a) \tag{2.42e}$$

$$a_{13}^{'} = a_{21}^{'} = a_{22}^{'} = a_{33}^{'} = 0 \tag{2.42f}$$

and hence the general frequency equation reduces to

$$\begin{bmatrix} a_{11}^{'} & a_{12}^{'} \\ a_{31}^{'} & a_{32}^{'} \end{bmatrix} a_{23}^{'} = 0 \tag{2.43}$$

This Eqn. 2.43 tends to zero in two ways, either the value of the determinant is zero which corresponds to longitudinal modes or the value $a_{23}^{'}$ tends to zero. Computing the determinant of the $2x2$ matrix, we have the '"Pochhamer Frequency Equation"', which Pochhammer discovered in the year 1876, which is the frequency equation of the first longitudinal mode. It is given by Eqn. 2.44

$$\frac{2\alpha}{a}(\beta^2+\xi^2)J_1(\alpha a)J_1(\beta a) - (\beta^2-\xi^2)J_0(\alpha a)J_1(\beta a) - 4\xi^2\alpha\beta J_1(\alpha a)J_0(\beta a) = 0 \tag{2.44}$$

For n=0, we have from the Eqn. 2.38b as $u_\theta = 0$. Also we have from Eqn. 2.32b and Eqn. 2.32d the terms ψ_r and ψ_z tend to zero. ie.

$$\psi_z = \psi_r = 0$$

. The remaining displacements u_z and u_r can thus be described in terms of ϕ and ψ_θ using Eqn. 2.32a,Eqn. 2.32c,Eqn. 2.35 andEqn. 2.36c as

$$\phi = AJ_0(\alpha r)e^{i(\xi z - \omega t)} \tag{2.45a}$$

$$\psi_\theta = -B_2 J_1(\beta r)e^{i(\xi z - \omega t)} \tag{2.45b}$$

Finally the displacements can be written as

$$u_r = B_2\{-\frac{A}{B_2}\alpha J_1(\alpha r) + i\xi J_1(\beta r)\}e^{i(\xi z-\omega t)} \tag{2.46a}$$

$$u_z = B_2\{\frac{A}{B_2}i\xi J_0(\alpha r) - \beta J_0(\beta r)\}e^{i(\xi z-\omega t)} \tag{2.46b}$$

where

$$\frac{A}{B_2} = -\frac{\beta}{\alpha}(\frac{\beta^2-\xi^2}{2\xi^2}\frac{J_1(\beta a)}{J_1\alpha a}) \tag{2.46c}$$

It is to be noted that the displacement and stress fields of the longitudinal mode are rotationally symmetric. This phenomenon of the longitudinal waves is fully exploited when we use Finite element methods (FEM), we use the symmetry property and reduce the calculation time. The concept of rotational symmetry for a longitudinal wave follows directly from the point that the displacements are independent on θ coordinate. The Eqn. 2.46 is difficult to solve numerically and hence we use the waveguide method [13] to view the displacements in the wavefront. This is shown in the last part of this section. It is also noted that the longitudinal waves that are propagating in a cylinder are similar to the symmetric and anti-symmetric lamb waves that propagate in a plate. The Section 2.2 gives in detail the lamb waves.

Torsional Waves

The torsional waves involve a circumferential displacement only which is independent of θ. [1]. It means that we assume the displacement u_θ exists. Such a displacement field is obtained only when $\psi_z \neq 0$ is assumed. Hence we have the following

$$\psi_z = B_3 J_0(\beta r)e^{i(\xi z-\omega t)} \tag{2.47a}$$

$$u_\theta = B J_1(\beta r)e^{i(\xi z-\omega t)} \tag{2.47b}$$

It is to be noted that we have replaced $-\beta B_3$ that results from differentiating $J_0\beta r$ by B in Eqn. 2.47b. The frequency for the torsional modes may be obtained by using the boundary condition $\sigma_{r\theta} = 0$ and noting from Eqn. 2.39b it is merely

$$r\frac{\partial}{\partial r}(\frac{u_\theta}{r}) = 0, \qquad r = a \tag{2.48}$$

This is equivalent of doing $a_{23}^{'} = 0$. Thus we have the torsional waves of the form

$$\beta a J_0(\beta a) = 2J_1(\beta a) \tag{2.49}$$

as the frequency equation for torsional waves. This frequency equation will also result if Eqn. 2.48 is solved directly. Some of the roots of the torsional wave frequency equation are

$$\beta_0 a = 0 \qquad \beta_1 a = 5.136 \qquad \beta_2 a = 8.417 \qquad \beta_3 a = 11.62...$$

. We also have a frequency-wave number relation as

$$(\beta a)^2 = (\frac{\omega a}{c_T})^2 - (\xi a)^2 \tag{2.50}$$

For the solution $\beta a = 0$ we examine the displacements $u_r = u_z = 0 \text{and} u_\theta = u_\theta(r, z)$ and find the only non trivial motion equation as

$$\frac{\partial^2 u_\theta}{\partial r^2} + \frac{1}{r}\frac{\partial u_\theta}{\partial r} - \frac{u_\theta}{r^2} + \frac{\partial^2 u_\theta}{\partial z^2} = \frac{1}{c_{\mathrm{T}}^2}\frac{\partial^2 u_\theta}{\partial t^2} \tag{2.51}$$

Considering a solution of the form $u_\theta = U(r)e^{i(\xi z - \omega t)}$ gives

$$\frac{d^2 U}{dr^2} + \frac{1}{r}\frac{dU}{dr} + (\beta^2 - \frac{1}{r^2})U = 0 \tag{2.52}$$

for $\beta = 0$, the resulting solution is

$$U = \frac{A}{r} + Br \tag{2.53}$$

The singular behaviour at $r = 0$ requires $A = 0$. Thus for $\beta = 0$, we have a displacement field given by,

$$u_\theta = Bre^{i(\xi z - \omega t)} \tag{2.54}$$

where $\xi = \frac{\omega}{c_{\mathrm{T}}}$. This denotes the lowest mode of propagation of torsional waves. It represents the exceptional case when strength of materials and elasticity yield the same results. This mode has a non dispersive propagation. As mentioned previously, it has the same frequency spectrum has the same shape as for the SH waves in a plate. Again, this mode is also plotted using the waveguide [13], even though the equations are quite easy to solve.

Flexural Waves

The flexural waves require all the components of displacements. Hence the case n=1 corresponds to the lowest order family of flexural modes. The displacement and frequency equations are more complicated than those for the longitudinal and torsional modes. Pao and Mindlin [9] have investigated the lowest branches of flexural modes, the resulting Pochhammer frequency equation is

$$J_1(\bar{\alpha})J_1^2\bar{\beta}(f_1\mathcal{J}_\beta^2 + f_2\mathcal{J}_\alpha\mathcal{J}_\beta + f_3\mathcal{J}_\beta + f_4\mathcal{J}_\alpha + f_5) = 0 \tag{2.55a}$$

where

$$f_1 = 2(\bar{\beta}^2 - \bar{\xi}^2)^2 \tag{2.55b}$$

$$f_2 = 2\bar{\beta}^2(5\bar{\xi}^2 + \bar{\beta}^2) \tag{2.55c}$$

$$f_3 = \bar{\beta}^2 - 10\bar{\beta}^4 - 2\bar{\beta}^4\bar{\xi}^2 + 2\bar{\beta}^2\bar{\xi}^2 + \bar{\beta}^2\bar{\xi}^4 - 4\bar{\xi}^4 \tag{2.55d}$$

$$f_4 = 2\bar{\beta}^2(2\bar{\beta}^2\bar{\xi}^2 - \bar{\beta}^2 - 9\bar{\xi}^2) \tag{2.55e}$$

$$f_5 = \bar{\beta}^2(-\bar{\beta}^4 + 8\bar{\beta}^2 - 2\bar{\beta}^2\bar{\xi}^2 + 8\bar{\xi}^2 - \bar{\xi}^4) \tag{2.55f}$$

where

$$\bar{\alpha} = \alpha a \qquad \bar{\beta} = \beta a \qquad \bar{\xi} = \xi a \qquad \Omega = \frac{\omega a}{c_{\mathrm{T}}} \qquad \mathcal{J}_x = xJ_0(x)/J_1(x) \tag{2.56}$$

We also plot the flexural waves in the following part.

2.3.3 Visualization of Wavefronts of Longitudinal, Torsional and Flexural Modes

As we can see, the wave number frequency relations for the longitudinal, torsional and flexural modes are very much complicated. To view the wavefronts.ie, the displacement regime that propagates in a direction, by which we can determine the type of wave, we use waveguide finite element method. This method has been designed by Mace et al [13]. It uses commercially available software packages to develop a single

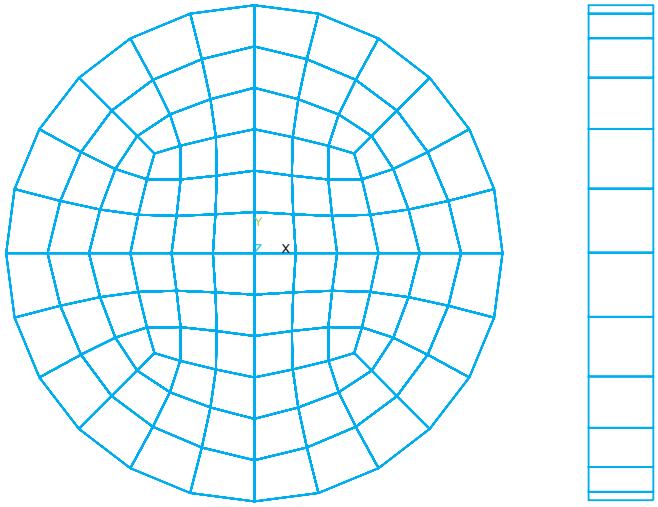

Figure 2.6: Finite Element Modelling of wave guide

section of the waveguide and then performs certain methods using the matrices and then get the waves that propagate in the cross section in the chosen direction. Here, a brief detail of the method and its implementation for our current problem is given. For other complex examples and numerical considerations, the reader is referred to the paper [13].

We use ANSYS® and MATLAB® to do the modelling and post processing respectively. For a cylinder, the cross section in which the wave propagates is circular in shape. It is noted that, we can see only longitudinal waves, in one-quarter of the model, a flexural and longitudinal wave in the half of the cross section and two flexural waves, a torsional wave and a longitudinal wave in the complete circular cross section. We model one section of the model as shown in Fig. 2.6 and Fig. 2.7, in ANSYS® and import the stiffness and mass matrix into MATLAB® using SDT toolbox. The conventional equations of motion become

$$(\mathbf{K} + i\omega\mathbf{C} - \omega^2\mathbf{M})\mathbf{u} = \mathbf{f} \tag{2.57}$$

where $\mathbf{K}$ is the stiffness matrix, $\mathbf{C}$ is the damping matrix ,$\mathbf{M}$ is the mass matrix,$\mathbf{f}$ is the vector of nodal forces and $\mathbf{u}$ is the vector of nodal degrees of freedom (DOF's). We now introduce a dynamic stiffness matrix $\tilde{\mathbf{H}} = \mathbf{K} + i\omega\mathbf{C} - \omega^2\mathbf{M}$ and the nodal forces and the DOF's are decomposed into sets associated with the right(R), interior(I) and left(L) nodes. We use a FE model with no interior nodes for ease of calculation, but now we can generally see how to tackle the interior nodes if modelled. For the case

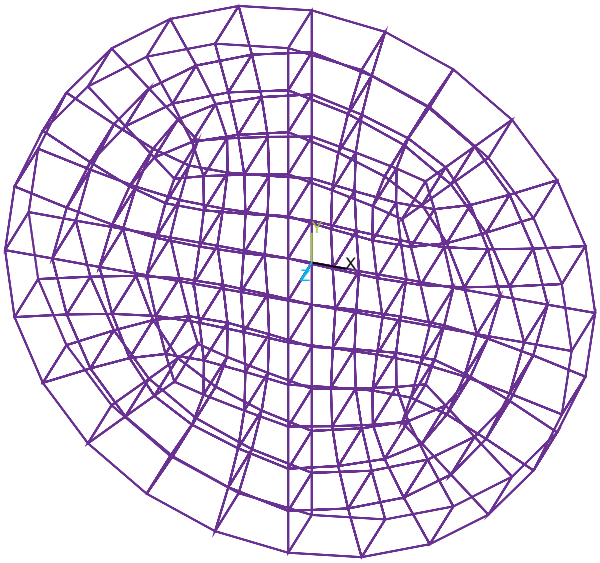

Figure 2.7: Finite Element Model of single section of the wave guide (Oblique View)

where there are no external forces on interior nodes, the equation of motion can be partioned as

$$\begin{bmatrix} \tilde{\mathbf{H}}_{II} & \tilde{\mathbf{H}}_{IL} & \tilde{\mathbf{H}}_{IR} \\ \tilde{\mathbf{H}}_{LI} & \tilde{\mathbf{H}}_{LL} & \tilde{\mathbf{H}}_{LR} \\ \tilde{\mathbf{H}}_{RI} & \tilde{\mathbf{H}}_{RL} & \tilde{\mathbf{H}}_{RR} \end{bmatrix} \begin{bmatrix} \mathbf{u}_I \\ \mathbf{u}_L \\ \mathbf{u}_R \end{bmatrix} = \begin{bmatrix} 0 \\ \mathbf{f}_L \\ \mathbf{f}_R \end{bmatrix} \tag{2.58}$$

From the Eqn. 2.58, it follows that the interior degrees of freedom as

$$\mathbf{u}_I = \tilde{\mathbf{H}}_{II}^{-1}(\tilde{\mathbf{H}}_{IL}\mathbf{u}_L + \tilde{\mathbf{H}}_{IR}\mathbf{u}_R) \tag{2.59}$$

These interior degrees of freedom can therefore be eliminated from Eqn. 2.58 as

$$\begin{bmatrix} \mathbf{H}_{LL} & \mathbf{H}_{LR} \\ \mathbf{H}_{RL} & \mathbf{H}_{RR} \end{bmatrix} \begin{bmatrix} \mathbf{u}_L \\ \mathbf{u}_R \end{bmatrix} = \begin{bmatrix} \mathbf{f}_L \\ \mathbf{f}_R \end{bmatrix} \tag{2.60}$$

where

$$\mathbf{H}_{LL} = \tilde{\mathbf{H}}_{LL} - \tilde{\mathbf{H}}_{LI}\tilde{\mathbf{H}}_{II}^{-1}\tilde{\mathbf{H}}_{IL} \qquad \mathbf{H}_{LR} = \tilde{\mathbf{H}}_{LR} - \tilde{\mathbf{H}}_{LI}\tilde{\mathbf{H}}_{II}^{-1}\tilde{\mathbf{H}}_{IR}$$

$$\mathbf{H}_{RL} = \tilde{\mathbf{H}}_{RL} - \tilde{\mathbf{H}}_{RI}\tilde{\mathbf{H}}_{II}^{-1}\tilde{\mathbf{H}}_{IL} \qquad \mathbf{H}_{RR} = \tilde{\mathbf{H}}_{RR} - \tilde{\mathbf{H}}_{RI}\tilde{\mathbf{H}}_{II}^{-1}\tilde{\mathbf{H}}_{IR}$$

Due to the symmetry of stiffness, mass and damping matrix, the dynamic stiffness

matrix is also symmetric. Hence we have the following relations true

$$\mathbf{H}_{LL}^T = \mathbf{H}_{LL}, \mathbf{H}_{RR}^T = \mathbf{H}_{RR}, \mathbf{H}_{LR}^T = \mathbf{H}_{RL}$$

where the superscript T indicates the transpose. Eqn. 2.60 forms the basis for the analysis of wave motion in a waveguide.

Suppose that no external forces are applied to the structure, and that the waveguide is divided into a number of similar sections. From continuity of displacements and equilibrium of forces at the cross-section between sections s and (s+1) it follows that

$$\mathbf{u}_L^{(s+1)} = \mathbf{u}_R^s \qquad \mathbf{f}_L^{(s+1)} = -\mathbf{f}_R^s \tag{2.61}$$

We introduce a transfer matrix ($\mathbf{T}$) that relates the nodal displacements and forces in cross-sections s and $(s+1)$. This matrix is defined such that

$$\begin{bmatrix} \mathbf{u}_L^{(s+1)} \\ \mathbf{f}_L^{(s+1)} \end{bmatrix} = \begin{bmatrix} \mathbf{u}_L^{(s)} \\ \mathbf{f}_L^{(s)} \end{bmatrix} \tag{2.62}$$

From Eqn. 2.60,Eqn. 2.61 and Eqn. 2.62, it follows that

$$\mathbf{T} = \begin{bmatrix} -\mathbf{H}_{LR}^{-1}\mathbf{H}_{LL} & \mathbf{H}_{LR}^{-1} \\ -\mathbf{H}_{RL} + \mathbf{H}_{RR}\mathbf{H}_{LR}^{-1}\mathbf{H}_{LL} & -\mathbf{H}_{RR}\mathbf{H}_{LR}^{-1} \end{bmatrix} \tag{2.63}$$

The transfer matrix $\mathbf{T}$ depends only on the dynamic stiffness of one section of the waveguide. When a free wave propagates along the waveguide, the displacements and forces at successive cross-sections are such that

$$\begin{bmatrix} \mathbf{u}_L^{(s+1)} \\ \mathbf{f}_L^{(s+1)} \end{bmatrix} = \lambda \begin{bmatrix} \mathbf{u}_L^{s} \\ \mathbf{f}_L^{s} \end{bmatrix} \tag{2.64}$$

Thus free wave propagation is described by the eigen problem

$$\mathbf{T} \begin{bmatrix} \mathbf{u}_L^{s} \\ \mathbf{f}_L^{s} \end{bmatrix} = \lambda \begin{bmatrix} \mathbf{u}_L^{s} \\ \mathbf{f}_L^{s} \end{bmatrix} \tag{2.65}$$

The 2n eigen values λ_j(j=1,2,....,2n) are related to the phase change over the length of the cross section Δ and the eigenvectors ϕ_j indicate the shape of the motion over the cross-section. Here n is the number of nodal DOF's on each side of the cross-section. The eigenvector can be partitione into n$\times$ 1 vectors associated with the nodal DOF's

and nodal forces, i.e,

$$\phi_j = \begin{Bmatrix} \phi_j^u \\ \phi_j^f \end{Bmatrix} \tag{2.66}$$

From the first row of the Eqn. 2.65 we have

$$\mathbf{f}_L = (\mathbf{H}_{LL} + \lambda \mathbf{H}_{LR})\mathbf{u}_L \tag{2.67}$$

and hence

$$\phi_j^f = (\mathbf{H}_{LL} + \lambda_j \mathbf{H}_{LR})\phi_j^u \tag{2.68}$$

If λ_j is an eigenvalue, so is $1/\lambda_j$. This follows by substituting Eqn. 2.67 in the second row of Eqn. 2.65, leads to after calculations

$$(\mathbf{H}_{LL} + \mathbf{H}_{RR} + \lambda \mathbf{H}_{LR} + \frac{1}{\lambda}\mathbf{H}_{RL})\mathbf{u}_L = 0 \tag{2.69}$$

The result follows by taking the transpose of this equation and noting the symmetric properties of the dynamic stiffness matrices. Therefore the eigenvalues of $\mathbf{T}$ are defined such that

$$|\lambda_j| \leq 1 \tag{2.70}$$

$$Re\{\mathbf{f}_L^H \dot{\mathbf{u}}_L\} = Re\{i\omega \mathbf{f}_L^H \mathbf{u}_L\} < 0 \qquad if \quad |\lambda_j| = 1 \tag{2.71}$$

The eigen solutions therefore come in two sets whose eigen values are (λ_j, ϕ_j^+) and $1/\lambda_j, \phi_j^-$ and which represent n positive-going and n negative-going wave types respectively. Eqn. 2.71 that either the amplitude of the wave decreases in the direction of propagation or that, if the amplitude remains constant, there is a time average power transmission in the direction of propagation. The jth eigenvalue can be written as

$$\lambda_j = e^{-ik_j\Delta} = e^{-\mu_j\Delta}e^{-ik_j'\Delta} \tag{2.72}$$

where the wave number can be complex. $k_j = k_j' - i\mu_j$ may be complex and where μ_j and k_j' are real and equal to the attenuation and phase change per unit length that is associated with the jth wave type.

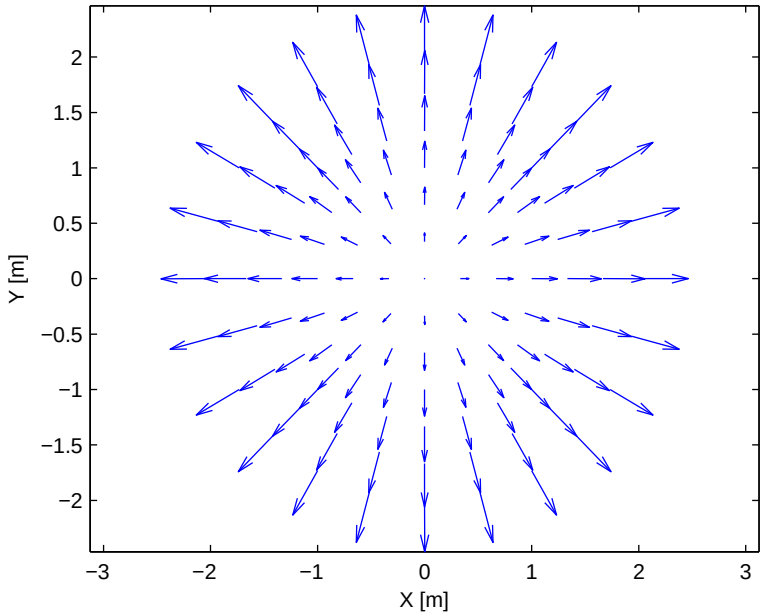

Figure 2.8: Wavefront of Longitudinal Waves

The Eqn. 2.72 is used in calculating the wavenumber k which is in turn used to determine the type of the wave that is propagating in the cross-section. Below is a list that gives the types of wave that occur and their direction of propagation in the medium based on the wavenumbers.

Wave propagation to left side of the cross-section $k^{'} < 0 \quad and \quad \mu = 0$

Wave propagates to the right side of the cross-section$k^{'} > 0 \quad and \quad \mu = 0$

Evanescent waves in the left side of the cross-section $k^{'} < 0 \quad and \quad \mu < 0$

Evanescent waves in the right side of the cross-section $k^{'} > 0 \quad and \quad \mu < 0$

Exponential waves in the left side$k^{'} < 0 \quad and \quad \mu > 0$

Exponential waves in the right side$k^{'} > 0 \quad and \quad \mu > 0$

Decaying waves $k^{'} = 0$

Waves formed due to numerical considerations $k^{'} * \Delta > \pi$

Thus these are the wave types that are generated. Now we need to calculate the displacement and the stress fields of the waves. We also need to find which propagating wave corresponds to which mode of transmission. We use the Eqn. 2.66

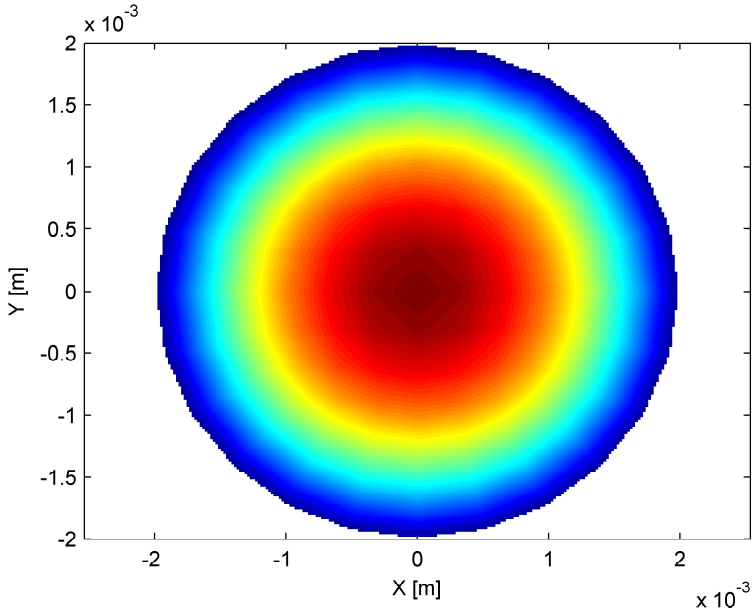

Figure 2.9: Wavefront of Longitudinal Waves

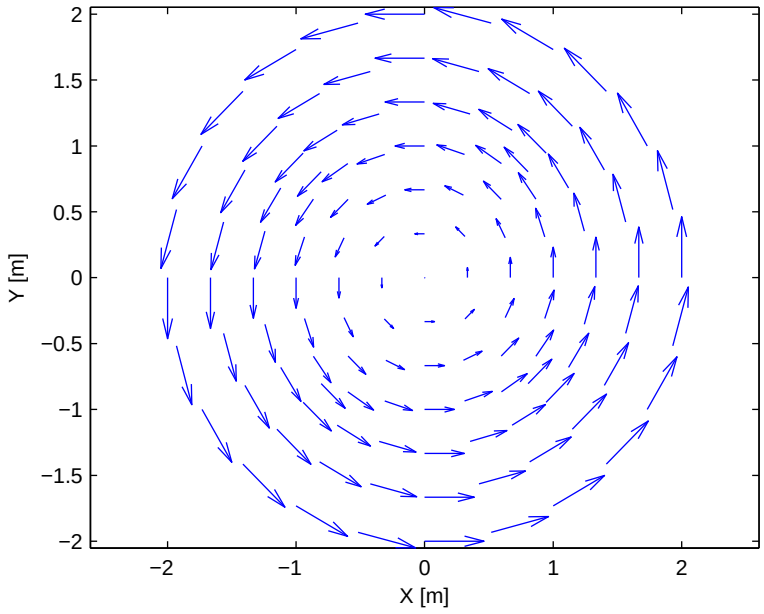

Figure 2.10: Wavefront of Torsional Waves

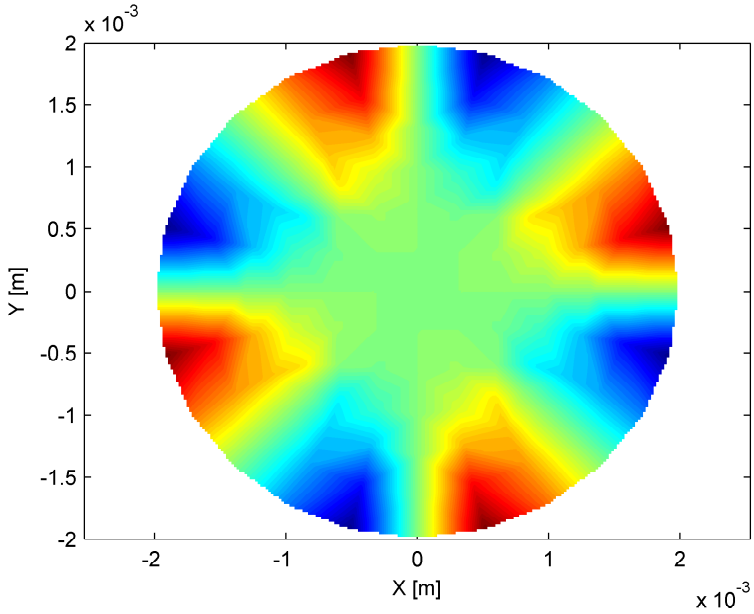

Figure 2.11: Wavefront of Torsional waves

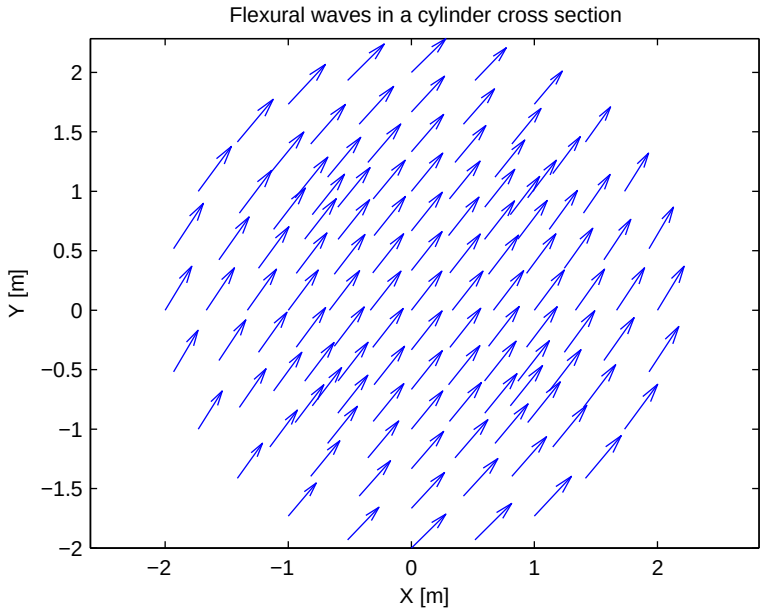

Figure 2.12: Wavefront of Flexural waves

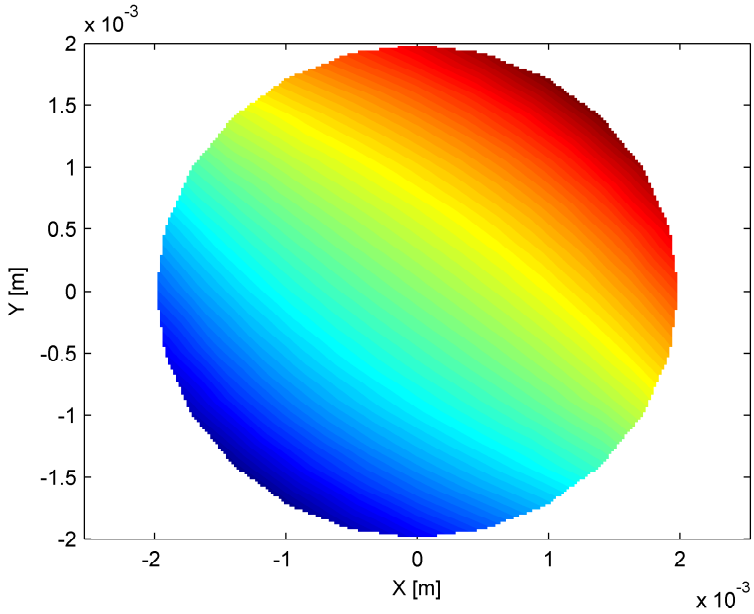

Figure 2.13: Wavefront of Flexural waves

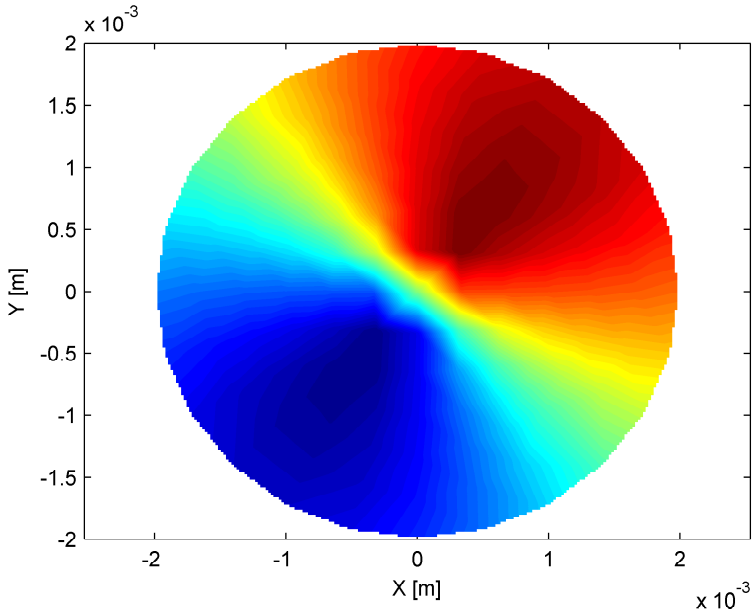

Figure 2.14: Wavefront of Flexural waves in u(r)

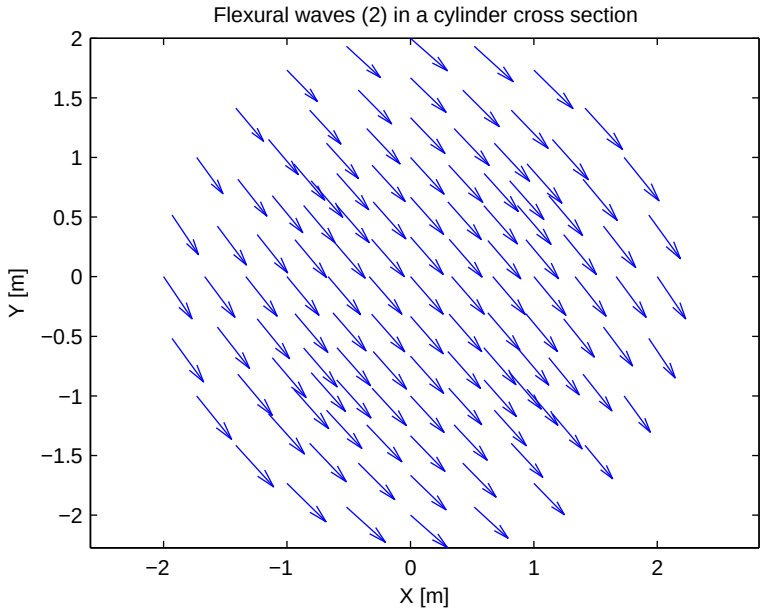

Figure 2.15: Wavefront of Flexural waves

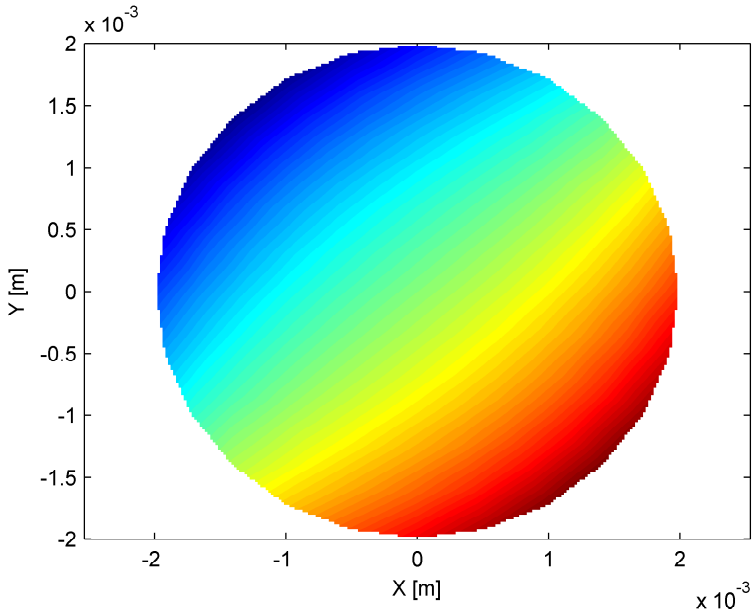

Figure 2.16: Wavefront of Flexural waves(2) in u(z)

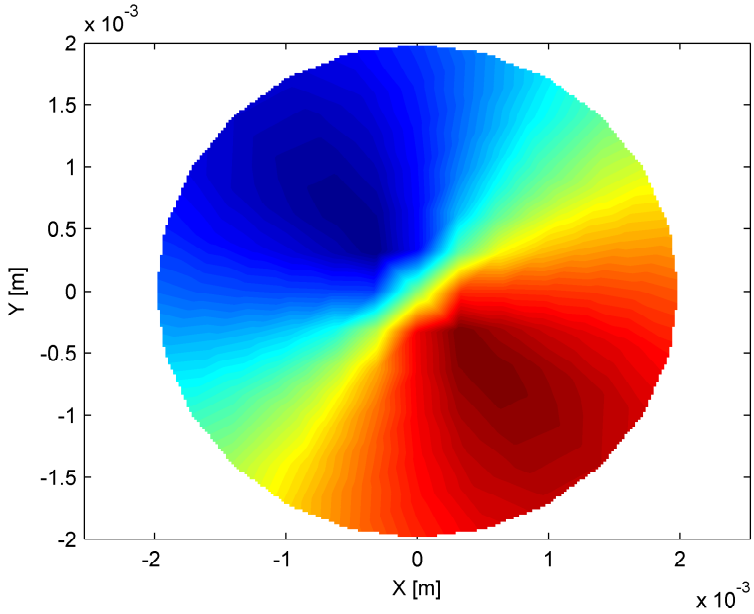

Figure 2.17: Wavefront of Flexural waves(2) in u(r)

to calculate the nodal DOFs and nodal forces. The partition of the eigenvectors gives the nodal forces and nodal DOFs on the left hand side of the model. Using the transformation matrix $\mathbf{T}$ we find out the nodal DOFs in the right hand side. It is given as $\mathbf{u}_R = \lambda \mathbf{u}_L$. Thus the displacements can be calculated. To distinguish the type of the waves, it is easy to use the displacements we have found out and assign the type accordingly. The total number of waves generated using the method is equal to the number of DOFs. The finite element model uses a circular cross-section of radius 2e-4 m and frequency of operation is 240 khz. So, since all the wavefronts are vectors, they have an amplitude and a direction of propagation. The flexural waves alone travel in radial and also in the z direction. We can see figures one by one. Fig. 2.8 shows the longitudinal waves in a cylinder, this figure shows the direction of the particles and Fig. 2.9 shows the amplitude of these waves. It is in the order of -5 to 5 e-8 m. Fig. 2.10 shows the direction of motion of the particles in a torsional wave. Fig. 2.11 shows the amplitude of the torsional wave in the radial direction, it is in the range of -8 to 8 e-12. So eventhough it has red regions in its figure, acutally it is just denotes higher displacements in those regions compared to others, but generally its displacement value is too low compared to the other modes. There are two types of flexural modes occuring in the cross-section and both are presented here to enable better understanding. Fig. 2.12 and Fig. 2.15 represent the directions of the two

flexural waves. Fig. 2.13 and Fig. 2.16 represents the displacement amplitude of the flexural waves in the z direction. Fig. 2.14 and Fig. 2.17 represent the amplitudes of displacement in the radial direction of the cylinder.

3 Modelling of Piezoelectric Transducer

The longitudinal waves in a cylinder and the lamb waves in a plate can be generated using a variety of contact and non contact methods. Of all the possible methods, the piezoelectric transducer based contact generation works well for our problem and is also cost effective. In this chapter, we can concentrate on modelling the piezoelectric transducer as an actuator for generating the longitudinal waves in the cylinder.

3.1 Piezoelectric Material

In the year 1880, Jaques and Pierre Curie, described the direct piezoelectric effect where a surface charge is generated as a result of mechanically straining the piezoelectric material. This is used for piezoelectric sensors, such as force and acceleration sensors. The inverse piezoelectric effect involves a change of geometry of the piezoelectric material as a result of applied electric field. Here we use this actuator effect of the piezoelectric material to generate the longitudinal waves.

The commonly available piezoelectric ceramic is PZT (lead - zirconate - titanate). PZT is a ferroelectric, polycrystalline material which showas a 100 larger inverse piezo electric effect than a monocrystalline quartz (SiO_2) material. The direct and inverse piezoelectric effects are based on an asymmetry of the crystalline elementary cell. This lack of symmetry is responsible for piezoelectric properties in 20 of the 32 crystalline categories. Pyro-electric materials, a sub group of piezoelectric materials, show a temperature dependent spontaneous polarization under uniform heating. A ferri-electric material is a pyro-electric material, whose polarization direction can be changed using an applied external electric field. The elementary cells of PZT mixture have a 'Perowskit'-structure.(Fig 3.1). The zirconium(Zr^{4+})or titanium(Ti^{4+})$-$ ion is body-centered, the lead- ions(Pb^{2+})are located at the edges of the elementary cells and the oxygen-ions are placed face-centred. Above the Curie-temperature T_C, PZT has a cubic lattice-structure,with the Zr^{4+} or Ti^{4+} ion placed at the centre of the cell. This configuration does not exhibit any piezoelectric properties. Below T_C, depending

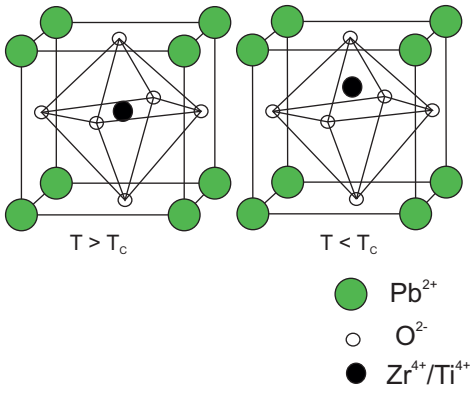

Figure 3.1: Perowskit-lattice of PZT ceramics

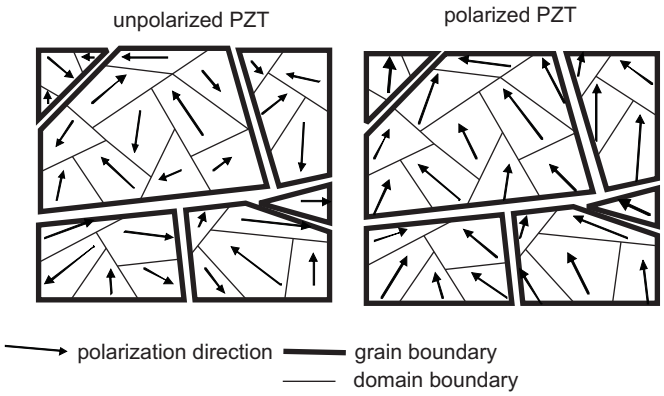

Figure 3.2: Domain Orientation at polarization of PZT

on the mixture ratio of zirconium and titanium, tetragonal or rhomboidal distorted mesh effects arise, whereby the $Zr^{4+}/Ti^{4+}-$ ions are no longer body-centred.

Each molecule has a polarization, ie, one end is more negatively charged and the other end is positively charged, and is called a dipole. This is a result of the atoms that make up the molecule and the way the molecules are shaped. The polar axis is an imaginary line that runs through the centre of both charges on the molecule. In a mono crystal the polar axes of all the dipoles lie in one direction. In a poly crystal, there are different regions within the material that have different polar axis. This can be seen in the figure (Fig 3.2).

PZT is a poly-crystalline material in which crystallites (d$\approx$ 1....10μ m) are ran-

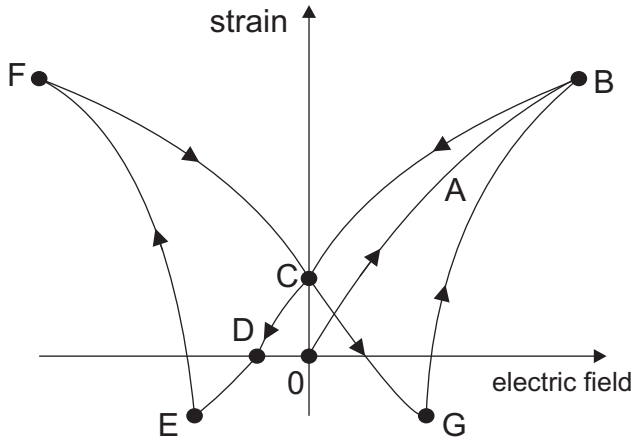

Figure 3.3: Bipolar Hysteresis of PZT

domly placed. These crystallites consist of a regular alignment of elementary-cells. Every elementary-cell of a grain affects the others; for this reason domains of uniform polarity arise for $T < T_C$. A single grain can posses one or more uniformly polarized domains. In the unimproved state, the polarization directions (Fig 3.2), whereby the polar axes are mostly oriented parallel to the electric field. After removing the electric field, a residual polarization of the material remains. This effect can be used to polarize PZT.

The strain-electric field correlation - a bipolar hysteresis - is plotted. An increase of the electric field yields from 0 to B. The slope of the curve decreases due to saturation (A) of the flip over process. The maximal field strength at B is limited by the electrical puncture resistance of the material. For PZT, the ultimate active strain is about 0.12%. A certain deformation remains after removal of the electric field due to remnant polarization(C). Applying a negative field leads to a state of no elongation of the ceramics (D)(coercive field strength). A further increase in the negative electric field leads to a contraction of the ceramic. It reaches a minimum when most of the dipoles have changed their polarity. Further increase of the negative electric field leads to an elongation of the material. The maximal stretch of the ceramic is found at F (electrical puncture of the material). From F to G the same behaviour as B to E is found. It is depicted in Fig. 3.3 Normally PZT-actuators are actuated unipolar and not bipolar. In this case, only a simple hysteresis is obtained as shown in Fig. 3.4. Further non linear effects are relaxation (creeping, drift) and electrostriction. Application of a constant electric field can lead to relaxation phenomena. After a rapid elongation, ceramics creep to an asymptotic value in about 100s. This effect

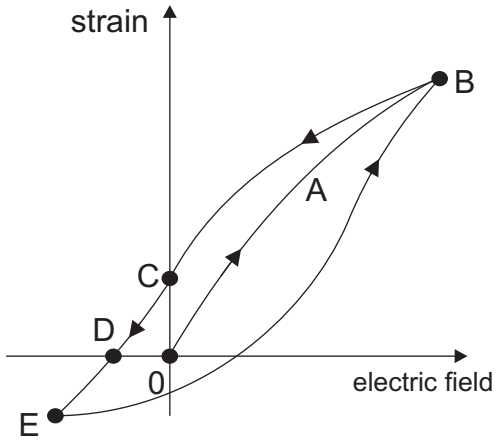

Figure 3.4: Unipolar Hysteresis of PZT

stems for a delayed flip-over process and a growth of some domains.

3.2 Material Law of Piezoelectric Ceramics

Most properties of materials are directional. In Cartesian coordinate system, depicted in the Fig. 3.5, the polarization direction is aligned parallel to the 3-axis. The 1- and 2- axes indicate the lateral directions; the coordinates 4 to 6 describe the rotation around the axes. PZT-ceramics are isotropic in the 1,2 -plane. PZT cermaics can be used as actuators in three different modes.

33-mode (elongation parallel to the applied electric field)

31-mode (stretch across the electric field)

15-mode(electric field perpendicular to the polarization direction, shear-strain in the transverse plane)

Piezo-stacks are composed of many ceramic plates glued together. They are electrically driven in parallel and are actuated in the 33-mode. The 31-effect is used for piezoceramic plate actuators which are fixed on a base structure or imbedded in a multilayer composite. Due to the isotropic behaviour in the 1,2 -directions in the PZT-plate, and electric field in the 3-direction induces an equal elongation in both cross directions. Fig 3.6 indicates the main 3 piezo actuator schemes.

In our problem, we will mainly use the 33-mode of actuation of the piezoelectric ceramic as it produces the longitudinal wave. An overview of the different piezo actuators is given in the figure below. We model the problem of the wire strands

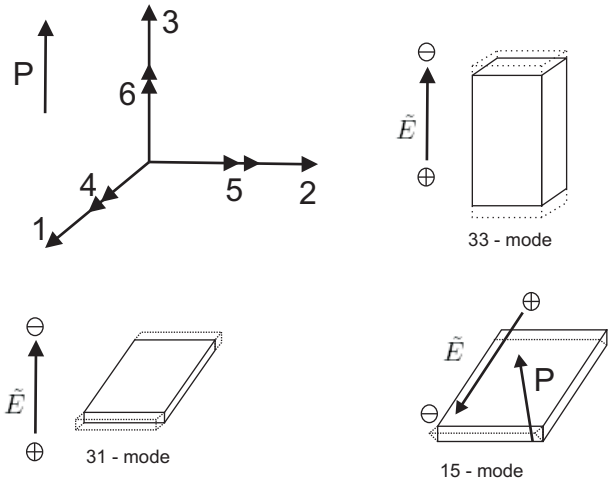

Figure 3.5: Different Modes of PZT

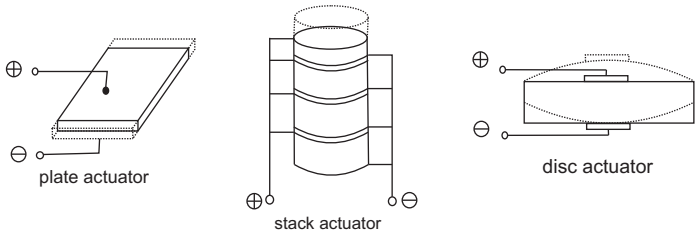

Figure 3.6: Different Shapes of piezo actuators

with two different shapes of piezo actuator. We use the disc-actuator and model it at the end of the wire or we use a plate-actuator and use it on the top and bottom of the wire. The stresses, strains, electric field and electric displacements in a piezoelectric material can be fully described in the linear range by a single set of electromechanical equations. Using a modified notation from the IEEE Standard 176-1987, the following two pairs of equations are equivalent statements which describe the electromechanical behaviour of a PZT element.

$$\epsilon_{ij} = s^{\tilde{E}}_{ijkl}\sigma_{kl} + d_{kij}\tilde{E}_k \tag{3.1}$$

$$\tilde{D}_j = d_{jkl}\sigma_{kl} + \tilde{\epsilon}^{\sigma}_{jk}\tilde{E}_k \tag{3.2}$$

and

$$\sigma_{ij} = c^{\tilde{E}}_{ijkl}\epsilon_{kl} - e_{kij}\tilde{E}_k \tag{3.3}$$

$$\tilde{D}_i = e_{ikl}\epsilon_{kl} + \tilde{\epsilon}^{\epsilon}_{ik}\tilde{E}_k \tag{3.4}$$

where ϵ_{ij} is the strain tensor, σ_{kl} is the stress tensor, $s^{\tilde{E}}_{ijkl}$ is the compliance tensor, d_{kij} and e_{ikl} are piezoelectric constants, $\tilde{E}_k$ is the electric field, $\tilde{D}_j$ is the dielectric displacement,$\tilde{\epsilon}^{\sigma}_{ik}$ is the permittivity and c_{ijkl} is the elasticity tensor. The superscripts $\tilde{E}$ and σ indicate that the values of the constants are obtained at constant electric field and constant electric stress, respectively. Eqn. 3.1 states that the strain in the piezoelectric material is proportional to both the applied stress (equivalent to the inverse of Hooke's law) and the applied electric field (the inverse piezoelectric effect). Eqn. 3.2 states that the electric displacement is proportional to both the applied stress (piezoelectric effect) and the applied piezoelectric field (dielectric effect). Eqn. 3.3 and Eqn. 3.4 are physically equivalent to Eqn. 3.1 and Eqn. 3.2. However, the permittivity in Eqn. 3.4 is measured at constant strain, and in Eqn. 3.2 it is measured at constant stress.

By arranging stress and strain components in vectors and assuming that the piezoelectric material is electrically and mechanically isotropic in the 1-2 plane (with the 3 axis parallel to the polarization axis), one obtains the constitutive equations in matrix notation.

$$\begin{bmatrix} \epsilon_{11} \\ \epsilon_{22} \\ \epsilon_{33} \\ \epsilon_{23} \\ \epsilon_{13} \\ \epsilon_{12} \\ \tilde{D}_1 \\ \tilde{D}_2 \\ \tilde{D}_3 \end{bmatrix} = \begin{bmatrix} s^{\tilde{E}}_{11} & s^{\tilde{E}}_{12} & s^{\tilde{E}}_{13} & 0 & 0 & 0 & 0 & 0 & d_{31} \\ s^{\tilde{E}}_{12} & s^{\tilde{E}}_{11} & s^{\tilde{E}}_{13} & 0 & 0 & 0 & 0 & 0 & d_{31} \\ s^{\tilde{E}}_{13} & s^{\tilde{E}}_{13} & s^{\tilde{E}}_{33} & 0 & 0 & 0 & 0 & 0 & d_{33} \\ 0 & 0 & 0 & s^{\tilde{E}}_{44} & 0 & 0 & 0 & d_{15} & 0 \\ 0 & 0 & 0 & 0 & s^{\tilde{E}}_{44} & 0 & d_{15} & 0 & 0 \\ 0 & 0 & 0 & 0 & 0 & s^{\tilde{E}}_{66} & 0 & 0 & 0 \\ 0 & 0 & 0 & 0 & d_{15} & 0 & \tilde{\epsilon}^{\sigma}_{11} & 0 & 0 \\ 0 & 0 & 0 & d_{15} & 0 & 0 & 0 & \tilde{\epsilon}^{\sigma}_{11} & 0 \\ d_{31} & d_{31} & d_{33} & 0 & 0 & 0 & 0 & 0 & \tilde{\epsilon}^{\sigma}_{33} \end{bmatrix} \begin{bmatrix} \sigma_{11} \\ \sigma_{22} \\ \sigma_{33} \\ \sigma_{23} \\ \sigma_{13} \\ \sigma_{12} \\ \tilde{E}_1 \\ \tilde{E}_2 \\ \tilde{E}_3 \end{bmatrix} \tag{3.5}$$

or equivalently

$$\begin{bmatrix}\sigma_{11}\\ \sigma_{22}\\ \sigma_{33}\\ \sigma_{23}\\ \sigma_{13}\\ \sigma_{12}\\ \tilde{D}_1\\ \tilde{D}_2\\ \tilde{D}_3\end{bmatrix} = \begin{bmatrix} c_{11}^{\tilde{E}} & c_{12}^{\tilde{E}} & c_{13}^{\tilde{E}} & 0 & 0 & 0 & 0 & 0 & -e_{31}\\ c_{12}^{\tilde{E}} & c_{11}^{\tilde{E}} & c_{13}^{\tilde{E}} & 0 & 0 & 0 & 0 & 0 & -e_{31}\\ c_{13}^{\tilde{E}} & c_{13}^{\tilde{E}} & c_{33}^{\tilde{E}} & 0 & 0 & 0 & 0 & 0 & -e_{33}\\ 0 & 0 & 0 & c_{44}^{\tilde{E}} & 0 & 0 & 0 & -e_{15} & 0\\ 0 & 0 & 0 & 0 & c_{44}^{\tilde{E}} & 0 & -e_{15} & 0 & 0\\ 0 & 0 & 0 & 0 & 0 & c_{66}^{\tilde{E}} & 0 & 0 & 0\\ 0 & 0 & 0 & 0 & e_{15} & 0 & \tilde{\epsilon}_{11}^{\epsilon} & 0 & 0\\ 0 & 0 & 0 & e_{15} & 0 & 0 & 0 & \tilde{\epsilon}_{11}^{\epsilon} & 0\\ e_{31} & e_{31} & e_{33} & 0 & 0 & 0 & 0 & 0 & \tilde{\epsilon}_{33}^{\epsilon}\end{bmatrix} \begin{bmatrix}\epsilon_{11}\\ \epsilon_{22}\\ \epsilon_{33}\\ \epsilon_{23}\\ \epsilon_{13}\\ \epsilon_{12}\\ \tilde{E}_1\\ \tilde{E}_2\\ \tilde{E}_3\end{bmatrix} \tag{3.6}$$

For special geometries, the constitutive law can be further simplified. Thus, for piezoelectric plates which are then in the 3-direction, the following may be assumed:

$$\sigma_{33} = \sigma_{23} = \sigma_{31} = 0$$

(plane stress) and

$$\tilde{E}_1 = \tilde{E}_2 = 0$$

(electric field is applied in the 3 direction). Under this assumptions, Eqn. 3.5 and Eqn. 3.6 for thin piezo plates reduce to

$$\begin{bmatrix}\epsilon_{11}\\ \epsilon_{22}\\ \epsilon_{12}\\ \tilde{D}_3\end{bmatrix} = \begin{bmatrix} \frac{1}{E} & -\frac{\mu_{12}}{E} & 0 & d_{31}\\ -\frac{\mu_{12}}{E} & \frac{1}{E} & 0 & d_{31}\\ 0 & 0 & \frac{1+\mu_{12}}{E} & 0\\ d_{31} & d_{31} & 0 & \tilde{\epsilon}_{33}^{\epsilon}\end{bmatrix} \begin{bmatrix}\sigma_{11}\\ \sigma_{22}\\ \sigma_{12}\\ \tilde{E}_3\end{bmatrix} \tag{3.7}$$

and

$$\begin{bmatrix}\sigma_{11}\\ \sigma_{22}\\ \sigma_{12}\\ \tilde{D}_3\end{bmatrix} = \begin{bmatrix} \frac{E}{1-\mu_{12}^2} & \frac{\mu_{12}E}{1-\mu_{12}^2} & 0 & -e_{31}\\ \frac{\mu_{12}E}{1-\mu_{12}^2} & \frac{E}{1-\mu_{12}^2} & 0 & -e_{31}\\ 0 & 0 & \frac{E}{1+\mu_{12}} & 0\\ e_{31} & e_{31} & 0 & \tilde{\epsilon}_{33}^{\epsilon}\end{bmatrix} \begin{bmatrix}\epsilon_{11}\\ \epsilon_{22}\\ \epsilon_{12}\\ \tilde{E}_3\end{bmatrix} \tag{3.8}$$

respectively, where E is the Young's modulus and μ_{12} is Poisson's ratio for the piezoelectric material. For the case of piezoelectric beams (the plate is now also thin in

the 2-direction so that $\sigma_{22} = \sigma_{12} = 0$), Equations 3.7 and 3.8 reduce to

$$\epsilon_{11} = \frac{1}{E}\sigma_{11} + d_{31}\tilde{E}_3 \qquad \tilde{D}_3 = d_{31}\sigma_{11} + \tilde{\epsilon}^{\sigma}_{33}\tilde{E}_3 \tag{3.9}$$

or equivalently

$$\sigma_{11} = E\epsilon_{11} - e_{31}\tilde{E}_3 \qquad \tilde{D}_3 = e_{31}\epsilon_{11} + \tilde{\epsilon}^{\epsilon}_{33}\tilde{E}_3 \tag{3.10}$$

The governing equations for a 1-dimensional piezo rod which stretches in the 3-direction are

$$\epsilon_{33} = \frac{1}{E}\sigma_{33} + d_{33}\tilde{E}_3 \qquad \tilde{D}_3 = d_{33}\sigma_{33} + \tilde{\epsilon}^{\sigma}_{33}\tilde{E}_3 \tag{3.11}$$

or equivalently

$$\sigma_{33} = E\epsilon_{33} = e_{33}\tilde{E}_3 \qquad \tilde{D}_3 = e_{33}\epsilon_{33} + \tilde{\epsilon}^{\epsilon}_{33}\tilde{E}_3 \tag{3.12}$$

This completes the material law of the piezoelectrics.

3.3 Advantages and Disadvantages of Using Piezoelectric Transducers for Generation of Longitudinal waves

PZT materials are excellent in production of lamb waves and longitudinal waves. They are suitable for integration into host structure as an insitu generator. They have neglectable mass/volume. Their other advantages include excellent mechanical strength,wide frequency responses, low power consumption, acoustic impedences and low cost.

The disadvantages of using a PZT generator is that, it gernerates multiple modes. It is to be noted that the longitudinal mode alone is required for the NDT, but other modes like flexural, torsional also get generated. This can be avoided by suitable design. Since multiple modes are generated, sophisticated signal processing is also required. Also under large strains/voltages or under high temperature, they show some non-linear behaviour. They also have small driving force/displacement, brittleness, low fatigue life etc are other problems using them.

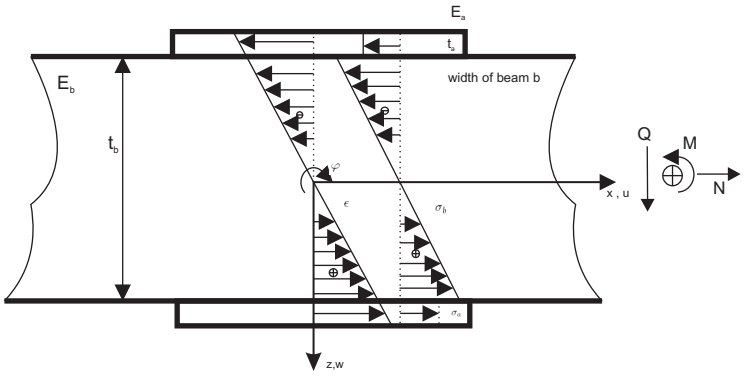

Figure 3.7: Euler-Bernoulli beam with piezo actuators (symmetric configuration)

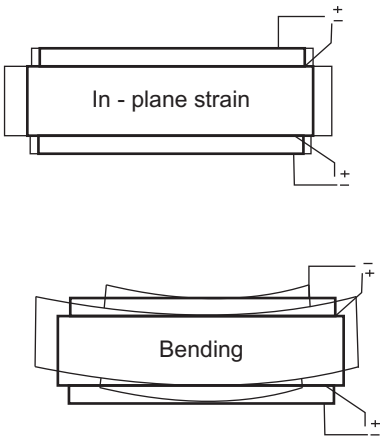

Figure 3.8: In-plane strain and bending effect of symmetric actuator arrangement

3.4 Modelling and Discretization of a Piezo Actuator

In this section, we can discuss the so called Euler-Bernoulli beam with piezo actuator. This concept is designed for a beam but can be extended to plates and shells as we can see in the later chapters. We use a linear piezoelectric mathematical model, the non linear effects like hysteresis are neglected.

The effect of piezoelectric actuators on composite beam structures may be described by a simplified model([2]) based on substitute forces and moments, so called equivalent actuator loads. Consider a host beam (index b) with attached piezoelectric actuators (index a) depicted in Fig. 3.7. The configuration is symmetric and the piezo actuators operate in $31-mode$, see Fig. 3.8

Identical driving voltage for both piezo actuators leads to a longitudinal(in-plane) effect. Oppostie sign of the driving voltages for the upper and lower piezos results in

a bending moment effect. Note the sign convention: a positive bending moment M leads to tensile stress ($\sigma > 0$) on the lower side of the beam (z>0).

Consider now the Euler-Bernoulli beam model depicted in Fig. 3.7 . The piezo actuators contribute to the total stiffness of the structure. Because the Euler-Bernoulli hypothesis is valid for the total composite consisting of active piezo layers and passive host structure, the strain varies linearly inside the piezos. The following relations for kinematics and material law are employed

$$\text{beam} \qquad \varepsilon_b = kz, \qquad \sigma_b = E_b \varepsilon_b \tag{3.13}$$

$$\text{piezo actuator} \qquad \varepsilon_a = kz, \qquad \sigma_a = E_a(\varepsilon_a - \Lambda) \tag{3.14}$$

It is to be noted that the in-plane strain is continuous but the stress is discontinuous at the interface between host beam and actuators. The moment equilibrium about z=0 is considered in order to determine the equivalent actuator moments. For this purpose, the stresses are integrated in thickness direction. Due to the symmetry of stresses for pure bending, it is sufficient to consider the lower half of the beam

$$\int_0^{t_b/2} \sigma_b z dz + \int_{t_b/2}^{t_a+t_b/2} \sigma_a z dz = M \tag{3.15}$$

Note that without external moment loads the moment balance is M=0 Substituting of Eqn. 3.13 and Eqn. 3.14 yields

$$\int_0^{t_b/2} E_b k z^2 dz + \int_{t_b/2}^{t_a+t_b/2} E_a(kz^2 - \Lambda z) dz = 0 \tag{3.16}$$

The result of the analytical integration of Eqn. 3.16 may be solved for the curvature k. After some transformations, we obtain

$$k = \frac{12}{t_b} \frac{1+\rho}{\psi + 6 + 12\rho + 8\rho^2} \Lambda \tag{3.17}$$

3.4.1 Coupled Electro - Mechanical Formulation

The kinematics of a composite beam structure according to Fig. 3.7 may be expressed in terms of bending and in-plane displacements

$$\varphi_{,x} + k = 0 \qquad w_{,x} - \varphi = 0 \tag{3.18}$$

From the above two equations, we can conclude that

$$w_{,xx} + k = 0 \tag{3.19}$$

Also

$$\varepsilon_0 = u_{,x} \tag{3.20}$$

The distribution in the thickness direction z of the total in-plane strain $\varepsilon(z)$ consists of two contributions, namely bending and in-plane strain

$$\varepsilon = kz + \varepsilon_0 \tag{3.21}$$

The corresponding equations of dynamic equilibrium are

$$Q_{,x} - \mu w_{,tt} + p_z = 0 \qquad M_{,x} - Q = 0 \tag{3.22a}$$

imply

$$M_{,xx} - \mu w_{,tt} + p_z = 0 \tag{3.22b}$$

$$N_{,x} - \mu u_{,tt} + p_x = 0 \tag{3.22c}$$

where the mass per unit length has been introduced according to

$$\mu = \sum_{k=1}^{n} \rho_k b_k (z_k - z_{k-1}) \tag{3.23}$$

The material law of the base/host structure (suffix b) corresponds to Hooke's law. For the piezo actuator or sensor layers (suffix p), the electromechanical coupling is considered in accordance with linear piezoelectricity which has been introduced earlier

$$\sigma_b = E_b \varepsilon \tag{3.24a}$$

$$\sigma_p = E_p(\varepsilon - d_{31}\tilde{E}) \tag{3.24b}$$

$$\tilde{D} = \tilde{\varepsilon}\tilde{E} + d_{31}\sigma_p \tag{3.24c}$$

In the case of actuators and sensors operating in 31-mode, the electric field is the derivative of the electric potential in thickness direction

$$\tilde{E} = -U_{,z} \tag{3.25}$$

Corresponding to the procedure of the classical laminated plate theory, the local stresses of all n material layers are integrated in thickness direction, and the total in -plane force N and the bending moment M are obtained

$$N = \int_{z_0}^{z_n} b(z)\sigma(z)dz = A\varepsilon_0 + Bk + \sum_{i=1}^{n_p} \lambda_i \int_{z_{k(i)-1}}^{z_{k(i)}} U_{,z}\, dz \tag{3.26a}$$

$$M = \int_{z_0}^{z_n} b(z)\sigma(z)zdz = B\varepsilon_0 + Dk + \sum_{i=1}^{n_p} \lambda_i \int_{z_{k(i)-1}}^{z_{k(i)}} U_{,z}\, zdz \tag{3.26b}$$

The summation in the last terms in the Eqn. 3.26 has to be carried out for all n_p piezo layers. Furthermore, the following abbreviations have been introduced in accordance with classical laminated plate theory.

$$\text{Membrane / in-plane stiffness} \qquad A = \sum_{k=1}^{n} b_k E_k (z_k - z_{k-1}) \qquad [\text{N}] \tag{3.27a}$$

$$\text{Coupling stiffness} \qquad B = \sum_{k=1}^{n} b_k E_k \frac{1}{2}(z_k^2 - z_{k-1}^2) \qquad [\text{Nm}] \tag{3.27b}$$

$$\text{Bending Stiffness} \qquad D = \sum_{k=1}^{n} b_k E_k \frac{1}{3}(z_k^3 - z_{k-1}^3) \qquad [\text{N}m^2] \tag{3.27c}$$

$$\text{Piezo coupling factor} \qquad \lambda_k = b_k E_k d_{31,k} \qquad [\text{N/V}] \tag{3.27d}$$

The equilibrium of the structure may be formulated in terms of the principle of virtual work, i.e., the sum of the contributions to the virtual work by the mechanical and electrical systems has to be zero

$$\delta A = \delta A_{\text{mech}} + \delta A_{\text{el}} = 0 \tag{3.28}$$

The virtual mechanical work is written by applying the displacement method,i.e the virtual displacements $\delta u, \delta w$, and $\delta\varphi$ are employed

$$\begin{aligned}\delta A_{\text{mech}} &= -\int_0^L \delta u \mu u_{,tt}\, dx - \int_0^L \delta w \mu w_{,tt}\, dx \\ &+ \int_0^L \delta u(N_{,x} + p_x)dx + \delta u(N - \bar{N})|_B \\ &+ \int_0^L \delta w(M_{,xx} + p_z)dx + \delta w(\bar{Q} - Q)|_B + \delta\varphi(M - \bar{M})|_B\end{aligned} \tag{3.29}$$

where the suffix B represents boundary terms. Integration by parts of the integrals invloving $\delta u N_{,x}$ and $\delta w M_{,xx}$ yields

$$\begin{aligned}\delta A_{\text{mech}} &= -\int_0^L \delta u \mu u_{,tt}\, dx - \int_0^L \delta w \mu w_{,tt}\, dx \\ &- \int_0^L \delta u_{,x}\, N dx + \int_0^L \delta y p_x dx - \delta u \bar{N}|_B \\ &+ \int_0^L \delta w_{,xx}\, M dx + \int_0^L \delta w p_z ds + \delta w \bar{Q}|_B - \delta\varphi \bar{M}|_B\end{aligned} \tag{3.30}$$

Substitution of the material laws and the kinematics gives the virutal mechanical work

$$\begin{aligned}-\delta A_{\text{mech}} &= \int_0^L \delta u \mu u_{,tt}\, dx + \int_0^L \delta u \mu u_{,tt}\, dx \\ &+ \int_0^L \delta u, x(Au_{,x} - Bw_{,xx})dx + \int_0^L \delta u_{,x} \sum_{i=1}^{n_p} \lambda_i \int_{z_{k(i)-1}}^{z_{k(i)}} U_{,z}\, dzdx \\ &- \int_0^L \delta w_{,xx}\,(Bu_{,x} - Dw_{,xx})dx - \int_0^L \delta w_{,xx} \sum_{i=1}^{n_p} \lambda_i \int_{z_{k(i)-1}}^{z_{k(i)}} U_{,z}\, zdzdx \\ &- \int_0^L \delta u p_x dx - \int_0^L \delta w p_z dx + \delta u \bar{N}|_B = \delta w \bar{Q}|_B + \delta\varphi \bar{M}|_B\end{aligned} \tag{3.31}$$

The virtual electrical work is formulated for each piezoelectric layer i. There are no electric charge source terms. Boundary conditions will be left out here and considered

after the discretization step in the following parts. Furthermore, no electric inertia termas are considered. The reasons for this are the fact that the speed of electromagnetic wave propagation in the piezo material is much faster than the elastic wave propagation in the structure. This means that the characteristic time scale of the piezo effect is far beyond the time scales of the elastic deformation of the beam which we are interested in. For this reason, the electrical work may be treated in quasi-state manner.

$$\begin{aligned}\delta A_{\mathrm{el}} &= \int_V \delta\tilde{E}\tilde{D}dV_i \\ &= \int_V (-\delta U_{,z})(\tilde{\varepsilon}_i - d_{31}^2 E_i)(-U_{,Z})dV_i + \int_{V_i} (-\delta U_{,z}))d_{31,i}E_i(u_{,x} - zw_{,xx})dV_i\end{aligned} \tag{3.32}$$

where V_i denotes the volume of the i-th piezo layer. Note that different virtual properties are employed for the mechanical $(\delta u, \delta w, \delta\varepsilon)$ and the electrical $(\delta\tilde{E}, \delta U)$ contributions to the virtual work. For this reason, the independant derivation of the mechanical and electrical terms is possible.

3.4.2 Finite Element Discretization of the Formulation

The total beam structure is subdivided into a number of elements of length l with end nodes A and B, see Fig.8. For the in-plane(longitudinal) displacements u linear interpolations are employed whereas Hermite polynomials of 3^{rd} order are used for the out-of-plane (bending) displacements w.

$$v = \begin{bmatrix} u \\ w \end{bmatrix} = \begin{bmatrix} \phi_1 & 0 & 0 & \phi_2 & 0 & 0 \\ 0 & \phi_3 & \phi_4 & 0 & \phi_5 & \phi_6 \end{bmatrix} \begin{bmatrix} u_A \\ w_A \\ \varphi_A \\ u_B \\ w_B \\ \varphi_B \end{bmatrix} = \phi\hat{\mathbf{v}} \tag{3.33}$$

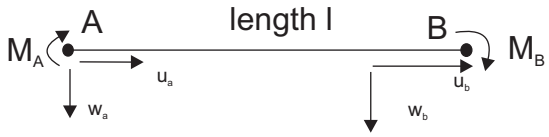

Figure 3.9: Finite element of a single piezo layer

The vector $\hat{\mathbf{v}}$ represents the mechanical nodal unknowns. The interpolations are

$$\begin{aligned} \phi_1 &= 1 - \frac{x}{l} \qquad \phi_3 = 1 - 3\frac{x^2}{l^2} + 2\frac{x^3}{l^3} \qquad \phi_5 = 3\frac{x^2}{l^2} - 2\frac{x^3}{l^3} \\ \phi_2 &= \frac{x}{l} \qquad \phi_4 = x - 2\frac{x^2}{l} \qquad \phi_6 = -\frac{x^2}{l} + \frac{x^3}{l^2} \end{aligned} \tag{3.34}$$

For the structural mechanics part, the displacement and strain distributions in thickness direction are obtained from the Euler-Bernoulli kinematics Eqn. 3.21 and the mechanical displacement unknowns need only be defined on the centre line of the composite beam. For the integration in thickness direction the analytical rules of the classical laminated plate theory Eqn. 3.27 are employed. The equations of piezoelectricity have to be dealt with differently because the field distribution in thickness direction is unknown and not given by any kinematics assumption. For this reason, the thickness direction has to be discretized. The interpolations for the electric potentials (voltage) U are chosen quadratic in order to obtain a linear electric field according to Eqn. 3.25. Fig. 3.9. depicts the finite element for one piezo layer. The resulting representation of electrical potential is

$$U_i = \begin{bmatrix} \psi_a & \psi_b & \psi_c & \psi_d & \psi_e & \psi_f \end{bmatrix} \begin{bmatrix} U_{ia} \\ U_{ib} \\ U_{ic} \\ U_{id} \\ U_{ie} \\ U_{if} \end{bmatrix} = \psi \hat{\mathbf{u}}_i \tag{3.35}$$

where $\hat{\mathbf{u}}_i$ is the vector of electric nodal unknowns of a single piezo layer element. The interpolations are in ξ, ζ -direction

$$\begin{aligned} \psi_a &= (\zeta^2 - \zeta)(1-\xi)/2 \qquad \psi_b = (\zeta^2 - \zeta)\xi/2 \qquad \psi_c = (1-\zeta^2)(1=\xi) \\ \psi_d &= (1-\zeta^2)\xi \qquad \psi_e = (\zeta^2 + \zeta)(1-\xi)/2 \qquad \psi_f = (\zeta^2 + \zeta)\xi/2 \end{aligned} \tag{3.36}$$

The local coordinates are defined as

$$\xi = \frac{x}{l} \qquad \zeta = \frac{2z - (z_{k(i)} + z_{k(i)-1})}{z_{k(i)} - z_{k(i)-1}} \tag{3.37}$$

The finite element interpolations given above are substituted to build the element virtual work terms in matrix formulation. Neglecting the boundary terms, the virtual mechanical work for an element of length l is

$$\begin{aligned} -\delta A_{\text{mech}} &= \int_0^l \delta \mathbf{v}^T \mu v_{,tt}\, dx + \int_0^l \delta \mathbf{v}^T \mathbf{D}^T \mathbf{E} \mathbf{D} \mathbf{v} dx \\ &+ \sum_{i=1}^{n_p} \int_0^l \delta \mathbf{v}^T \mathbf{D}^T \lambda_i \int_{z_{k(i)-1}}^{z_{k(i)}} \mathbf{G} U_{,z}\, dz dx - \int_0^l \delta \mathbf{v}^T \mathbf{p}_e dx \end{aligned} \tag{3.38}$$

where

$$\mathbf{D} = \begin{bmatrix} \partial_x & 0 \\ 0 & \partial_{xx} \end{bmatrix} \qquad \mathbf{E} = \begin{bmatrix} A & -B \\ =B & D \end{bmatrix} \qquad \mathbf{G} = \begin{bmatrix} 1 \\ -z \end{bmatrix} \qquad \mathbf{P}_e = \begin{bmatrix} p_x \\ p_z \end{bmatrix} \tag{3.39}$$

Substitution of the interpolations for u, w and U yields

$$\begin{aligned} -\delta A^E_{\text{mech}} &= \delta \hat{\mathbf{v}}^T [\int_0^l \phi^T \mu \phi dx \hat{\mathbf{v}}_{,tt} + \int_0^l \phi^T \mathbf{D}^T \mathbf{E} \mathbf{D} \phi dx \hat{\mathbf{v}} \\ &+ \sum_{i=1}^{n_p} \int_0^l \phi^T \mathbf{D}^T \lambda_i \int_{z_{k(i)-1}}^{z_{k(i)}} \mathbf{G} \psi_{,z} dz dx \hat{\mathbf{u}}_i - \int_0^l \phi^T \mathbf{p}_e dx] \end{aligned} \tag{3.40}$$

Thus from the above equation, we can see

$$-\delta A^E_{\text{mech}} = \delta \hat{\mathbf{v}}^T \left[\mathbf{m}_{vv} \hat{\mathbf{v}}_{,tt} + \mathbf{k}_{vv} \hat{\mathbf{v}} + \sum_{i=1}^{n_p} \mathbf{k}_{vu,i} \hat{\mathbf{u}}_i - \mathbf{p} \right] \tag{3.41}$$

where the element mass matrix $\mathbf{m}_{vv}$, the element stiffness matrix $\mathbf{k}_{vv}$, the electro-mechanical coupling matrix for the i-th piezo layer $\mathbf{k}_{vu,i}$ as well as the element load vector $\mathbf{p}$ have been introduced. Analytical integration yields the element mass matrix

$$\mathbf{m}_{vv} = \mu \begin{bmatrix} \frac{l}{3} & 0 & 0 & \frac{l}{6} & 0 & 0 \\ 0 & \frac{13l}{35} & \frac{11l^2}{210} & 0 & \frac{9l}{70} & -\frac{13l^2}{420} \\ 0 & \frac{11l^2}{210} & \frac{l^3}{105} & 0 & \frac{13l^2}{420} & -\frac{l^3}{140} \\ \frac{l}{6} & 0 & 0 & \frac{l}{3} & 0 & 0 \\ 0 & \frac{9l}{70} & \frac{13l^2}{420} & 0 & \frac{13l}{35} & -\frac{11l^2}{210} \\ 0 & -\frac{13l^2}{420} & -\frac{l^3}{140} & 0 & -\frac{11l^2}{210} & \frac{l^3}{105} \end{bmatrix} \tag{3.42}$$

and the element stiffness matrix

$$\mathbf{k}_{vv} = \begin{bmatrix} \frac{A}{l} & 0 & -\frac{B}{l} & -\frac{A}{l} & 0 & \frac{B}{l} \\ 0 & \frac{12D}{l^3} & \frac{6D}{l^2} & 0 & -\frac{12D}{l^3} & \frac{6D}{l^2} \\ -\frac{B}{l} & \frac{6D}{l^2} & \frac{4D}{l} & \frac{B}{l} & -\frac{6D}{l^2} & \frac{2D}{l} \\ -\frac{A}{l} & 0 & \frac{B}{l} & \frac{A}{l} & 0 & -\frac{B}{l} \\ 0 & -\frac{12D}{l^3} & -\frac{6D}{l^2} & 0 & \frac{12D}{l^3} & -\frac{6D}{l^2} \\ \frac{B}{l} & \frac{6D}{l^2} & \frac{2D}{l} & -\frac{B}{l} & -\frac{6D}{l^2} & \frac{4D}{l} \end{bmatrix} \tag{3.43}$$

In the mass matrix, the in-plane and the out-of-plane degrees of freedom are decoupled. The term of the stiffness matrix involving the stiffness B represents the coupling of in-plane and out-of-plane deformations according to the classical laminated plate theory. The electro-mechanical coupling matrix of the i-th element piezo layer reads

$$\mathbf{k}_{vv,i} = \lambda_i \begin{bmatrix} \frac{1}{2} & \frac{1}{2} & 0 & 0 & -\frac{1}{2} & -\frac{1}{2} \\ -\frac{C_1}{l} & \frac{C_1}{l} & -\frac{C_2}{l} & \frac{C_2}{l} & -\frac{C_3}{l} & \frac{C_3}{l} \\ -C_1 & 0 & -C_2 & 0 & -C_3 & 0 \\ -\frac{1}{2} & -\frac{1}{2} & 0 & 0 & \frac{1}{2} & \frac{1}{2} \\ \frac{C_1}{l} & -\frac{C_1}{l} & \frac{C_2}{l} & -\frac{C_2}{l} & \frac{C_3}{l} & -\frac{C_3}{l} \\ 0 & C_1 & 0 & C_2 & 0 & C_3 \end{bmatrix} \tag{3.44}$$

The constants

$$\begin{aligned} C_1 &= \frac{(z_{k(i)} + z_{k(i)-1})}{2} - \frac{(z_{k(i)} - z_{k(i)-1})}{3} \\ C_2 &= \frac{2(z_{k(i)} - z_{k(i)-1})}{3} \\ C_3 &= -\frac{(z_{k(i)} + z_{k(i)-1})}{2} - \frac{(z_{k(i)} - z_{k(i)-1})}{3} \end{aligned} \tag{3.45}$$

are obtained by analytical integration of the interpolations in the thickness direction of the piezo layer. Finally, the element load vector for linearly interpolated line loads is

$$\mathbf{p} = \begin{bmatrix} \frac{l}{3} & 0 & \frac{l}{6} & 0 \\ 0 & \frac{7l}{20} & 0 & \frac{3l}{20} \\ 0 & \frac{l^2}{20} & 0 & \frac{l^2}{30} \\ \frac{l}{6} & 0 & \frac{l}{3} & 0 \\ 0 & \frac{3l}{20} & 0 & \frac{7l}{20} \\ 0 & -\frac{l^2}{30} & 0 & -\frac{l^2}{20} \end{bmatrix} \begin{bmatrix} p_{xA} \\ p_{zA} \\ p_{xB} \\ p_{zB} \end{bmatrix} \tag{3.46}$$

Omitting boundary terms, the electrical virtual work of a piezo layer element may be written as

$$\delta A^E_{el} = (\tilde{\varepsilon}_i - d^2_{31} E_i) b_i \int_0^l \int_{z_{k(i)-1}}^{z_{k(i)}} \delta U_{,z}\, U_{,Z}\, dz dx - \lambda_i \int_0^l \int_{z_{k(i)-1}}^{z_{k(i)}} \delta U_{,z}\, \mathbf{G}^T dz \mathbf{D} \mathbf{v} dx \tag{3.47}$$

Substitution of the finite element interpolations of the mechanical and electrical unknowns yields

$$\begin{aligned} \delta A^E_{el} &= \delta \hat{\mathbf{u}}_i^T \left[\int_0^l \int_{z_{k(i)-1}}^{z_{k(i)}} {}^{,T}_{z} (\tilde{\varepsilon}_i - d^2_{31} E_i) b_{i,z}\, dz dx \hat{\mathbf{u}}_i - \int_0^l \lambda_i \int_{z_{k(i)-1}}^{z_{k(i)}} {}^{,T}_{z} \mathbf{G}^T dz \mathbf{D} dx \hat{\mathbf{v}} \right] \\ &= \delta \hat{\mathbf{u}}_i^T \left[\mathbf{k}_{uu,i} \hat{\mathbf{u}}_i - \mathbf{k}^T_{vu,i} \hat{\mathbf{v}} \right] \end{aligned} \tag{3.48}$$

The electromechanical coupling matrix $\mathbf{k}_{vu,i}$ has been given previously in Eqn. 3.44. As a result of the global conservation of work and globally conservative exchange of energy between the mechanical and the electrical systems, the electro-mechanical coupling terms of the Eqn. 3.41 and Eqn. 3.48 are "symmetric", i.e. $\mathbf{k}_{vu,i}$,does ap-

pear as negative transpose in Eqn. 3.48. This means that the electro-mechanical contribution to the structural energy is in turn removed from the electric system and global conservation is preserved for the finite element discretization. The matrix of electrostatics is

$$\mathbf{k}_{uu,i} = \frac{(\hat{\varepsilon} - d_{31}^2 E_i) b_i l}{18(z_{k(i)} - z_{k(i)-1})} \begin{bmatrix} 14 & 7 & -16 & -8 & 2 & 1 \\ 7 & 14 & -8 & -16 & 1 & 2 \\ -16 & -8 & 32 & 16 & -16 & -8 \\ -8 & -16 & 16 & 32 & -8 & -16 \\ 2 & 1 & -16 & -8 & 14 & 7 \\ 1 & 2 & -8 & -16 & 7 & 14 \end{bmatrix} \tag{3.49}$$

The matrix is singular which means that appropriate boundary conditions have to be introduced for the electric field of the piezo layers (in order to suppress electri "rigid body motion"). In the case of piezo actuators, the potential of nodes e and f is set to zero and the potential of nodes a and b is set to the prescribed voltage $\bar{U}$. For this purpose, the rows and columns of the coupling and electrostatics matrices corresponding to nodes e and f are eliminated. The prescribed voltages of nodes a and b appear as piezo load vectors for structural dynamics and electrostatics on the right hand side of the linear system of equations. Only nodal voltages U_{ic} and U_{id} at the centre nodes c and d remain unknown. For piezo layers employed as actuators, the reduced matrix and load vector of electrostatics are obtained

$$\mathbf{k}_{uv,i,A} = \frac{(\hat{\varepsilon} - d_{31}^2 E_i) b_i l}{9(z_{k(i)} - z_{k(i)-1})} \begin{bmatrix} 16 & 8 \\ 8 & 16 \end{bmatrix} \tag{3.50}$$

$$\mathbf{b}_{u,i} = \frac{4(\hat{\varepsilon} - d_{31}^2 E_i) b_i l}{3(z_{k(i)} - z_{k(i)-1})} \begin{bmatrix} 1 \\ 1 \end{bmatrix} \tag{3.51}$$

. The corresponding reduced electro-mechanical coupling matrix and piezo load vector for structural dynamics read

$$\mathbf{k}_{vu,i,A} = \lambda_i C_2 \begin{bmatrix} 0 & 0 \\ -\frac{1}{l} & \frac{1}{l} \\ -1 & 0 \\ 0 & 0 \\ \frac{1}{l} & -\frac{1}{l} \\ 0 & 1 \end{bmatrix} \qquad \mathbf{b}_{v,i} 0 \lambda_i \begin{bmatrix} -1 \\ 0 \\ C_1 \\ 1 \\ 0 \\ -C_1 \end{bmatrix} \tag{3.52}$$

The elements of the actuator load vector $\mathbf{b}_{v,i}$ demonstrate the effects of a piezo actuator layer: it generates both an in-plane force $N_\Lambda = \lambda_i \bar{U}_i$ as well as a bending moment $M_\Delta = C_1 \lambda_i \bar{U}_i$. Note that the moment arm C_1 according to Eqn. 3.45 of actuator layers that are symmetric to the neutral axis (z=0) is zero, resulting in-plane force. The element matrices derived above are assembled according to the topology of the composite beam discretization. The total system matrices of structural dynamics and electrostatics have the following dimensions.

$\mathbf{M}_{vv}$	$(n_v \times n_v)$	Mass matrix
$\mathbf{K}_{vv}$	$(n_v \times n_v)$	Stiffness matrix
$\mathbf{K}_{vu}$	$(n_v \times n_u)$	Electro-mechanical coupling matrix
$\mathbf{K}_{uu}$	$(n_u \times n_u)$	Electrostatics matrix
$\mathbf{P}$	$(n_v \times 1)$	Mechanical load vector
$\mathbf{b}_v$	$(n_v \times n_a)$	Actuator load vector of structural dynamics
$\mathbf{b}_u$	$(n_u \times n_a)$	Actuator load vector of elastostatics

The dimensions $n_v, n_u \text{and} n_a$ represent the number of system displacement and voltage unknowns and the number of independant piezo actuator layers, respectively. The total electro mechanical system reads

$$\begin{bmatrix} \mathbf{M}_{vv} & 0 \\ 0 & 0 \end{bmatrix} \begin{bmatrix} \bar{\mathbf{v}}_{,tt} \\ \bar{\mathbf{u}}_{,tt} \end{bmatrix} + \begin{bmatrix} \mathbf{K}_{vv} & \mathbf{K}_{vu} \\ -\mathbf{K}_{vu}^T & \mathbf{K}_{uu} \end{bmatrix} \begin{bmatrix} \bar{\mathbf{v}} \\ \bar{\mathbf{u}} \end{bmatrix} = \begin{bmatrix} \mathbf{b}_v \\ \mathbf{b}_u \end{bmatrix} \bar{\mathbf{U}} + \begin{bmatrix} \mathbf{P} \\ 0 \end{bmatrix} \tag{3.53}$$

where $\bar{\mathbf{v}}$ and $\bar{\mathbf{u}}$ are the vectors of mechanical and electrical nodal unknowns of the system and $\bar{\mathbf{U}}$ the vector of prescribed actuator voltages.

Thus we have the finite element model of the combined piezo- beam structure. It is directly extended to the 3-D case where, the nodal dof's point to the three dof's in a single node. Using the Eqn. 3.53, we can start the modelling of our problem in the next chapter.

4 Modelling of Wave Propagation

Once we have the basics of modelling a piezo and the physics behind the waves that are generated in the cylinder, we can look to model the wave propagation in the cylinder using piezoelectric transducers. A simple method for the use of piezoelectric transducers for the generation of waves is given by Nienwenhui.et.al [15]. We will use their methods for generating waves. Our model consists of strands of wires and a cross-section is like in Fig. 4.1.

For a structural health monitoring, we need to generate the longitudinal waves, with the help of piezo that travel over long distances. Once these waves are generated, a piezoelectric sensor is placed and the waves are monitored at a considerable distance from the generation point. In case any defect is present in the line, then there is reflection in the waves and the amplitude comes down. By monitoring this, we can predict the defects in the structure.

4.1 Finite Element Modelling of Guided Wave Propagation in 3D (Type 1)

Before starting the modelling, we must remember two important points

1. a fine FEM mesh featuring atleast 8-12 nodes per wavelength is a prerequisite to deliver good spatial precision. ([18])

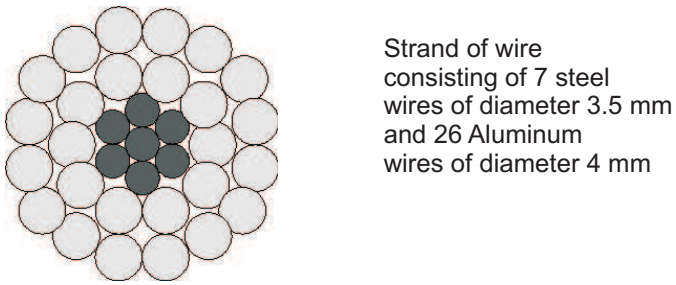

Figure 4.1: Cross-section of the wire strand

2. The time step for dynamic calculation should be less than the ratio of minimum distance of any two adjoining nodes to the maximum wave velocity (in our case the velocity of the longitudinal wave) ([17])

We also choose the longitudinal wave for detection of damage because of the following reasons

- Lower attenuation compared to other modes
- Faster wave propagation velocity
- Lower dispersion in the low frequency region, thereby helping in signal interpretation

We propose a setup with a circular piezo operating in the 33-mode. We use ANSYS® to model the proposed experimental setup. We use the property of symmetry to generate the longitudinal wave and import the model into MATLAB® to couple the electrical degrees of freedom as discussed below. The Fig. 4.2 shows the left view of the model as modelled in ANSYS®. The Fig. 4.3 shows the front view of the model and Fig. 4.4 shows the three-dimensional view of the model. The challenge in this modelling was to match the nodes in the circular faces as we had three different cross-sections. The challenge was successfully solved by meshing with area elements and then extruding for solid elements. The left end of the model had the piezo element and then the brass element and at last we had the cylinder made up of aluminium.

The material properties for alumnium cylinder that were used are

Young's Modulus	E	70.75 GPa
Poisson's Ratio	ν	0.3375
Density	ρ	2700 $\frac{kg}{m^3}$
Radius	r	2 mm

The material properties of the PZT material (PIC151) can be given in the form of matrices directly referring to the equations in the previous chapter (Eqn. 3.3 , Eqn. 3.4 and Eqn. 3.6). The stress compliance matrix $c_{ijkl}^{\tilde{E}}$ is given by

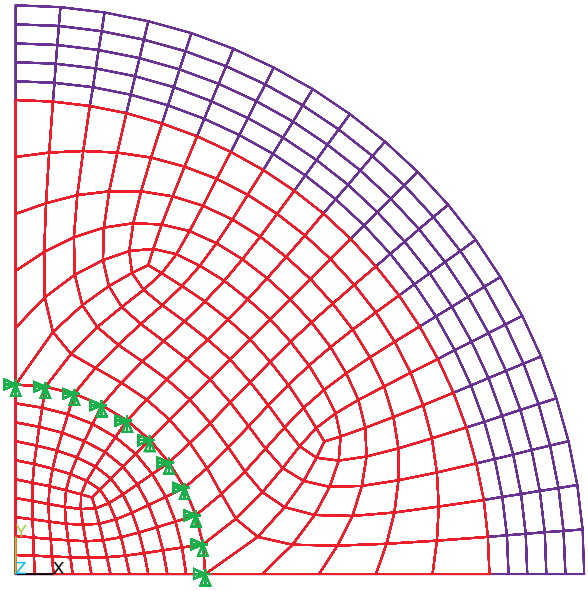

Figure 4.2: Left View of Type1 Model

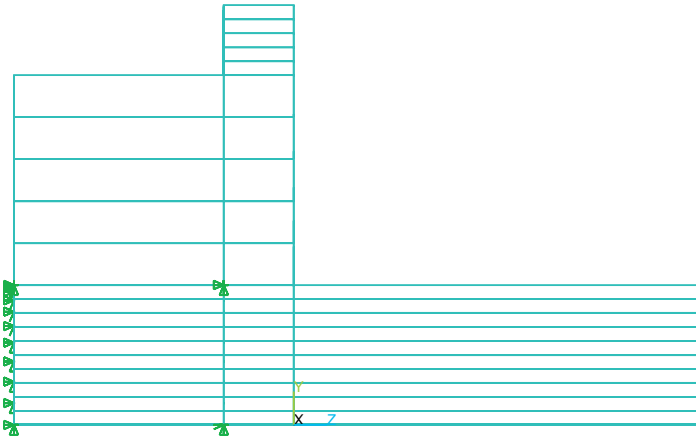

Figure 4.3: Front View of Type1 Model

$$\left[c^{\tilde{E}}\right] = \begin{bmatrix} c_{11}^{\tilde{E}} & c_{12}^{\tilde{E}} & c_{13}^{\tilde{E}} & 0 & 0 & 0 \\ & c_{11}^{\tilde{E}} & c_{13}^{\tilde{E}} & 0 & 0 & 0 \\ & & c_{33}^{\tilde{E}} & 0 & 0 & 0 \\ & & & c_{44}^{\tilde{E}} & 0 & 0 \\ & & & & c_{44}^{\tilde{E}} & 0 \\ & & & & & c_{66}^{\tilde{E}} \end{bmatrix} = 10^{10} \begin{bmatrix} 10.76 & 6.312 & 6.385 & 0 & 0 & 0 \\ & 10.76 & 6.385 & 0 & 0 & 0 \\ & & 10.04 & 0 & 0 & 0 \\ & & & 1.962 & 0 & 0 \\ & & & & 1.962 & 0 \\ & & & & & 2.224 \end{bmatrix}$$

The piezoelectric matrix at constant strain e_{ikl} can be written in matrix form as

$$\left[e\right]^{\mathrm{T}} = \begin{bmatrix} 0 & 0 & e_{31} \\ 0 & 0 & e_{31} \\ 0 & 0 & e_{33} \\ 0 & 0 & 0 \\ 0 & e_{15} & 0 \\ e_{15} & 0 & 0 \end{bmatrix} = 10^{-12} * \begin{bmatrix} 0 & 0 & -214 \\ 0 & 0 & -214 \\ 0 & 0 & 423 \\ 0 & 610 & 0 \\ 610 & 0 & 0 \end{bmatrix}$$

Similarly the permittivity $\tilde{\epsilon}_{ik}^{\epsilon}$ can be written as

$$\left[\tilde{\epsilon}^{\epsilon}\right] = \begin{bmatrix} \tilde{\epsilon}_{11}^{\epsilon} & 0 & 0 \\ 0 & \tilde{\epsilon}_{11}^{\epsilon} & 0 \\ 0 & 0 & \tilde{\epsilon}_{33}^{\epsilon} \end{bmatrix} = \begin{bmatrix} 1936 & & \\ & 1936 & \\ & & 2109 \end{bmatrix}$$

The density of the PIC151 material is given as $\rho = 7760\frac{kg}{m^3}$ .The piezo was circular in shape with a diameter of 5 mm and thickness of 2 mm . The aluminium culinder had a radius of 2 mm and was modelled for a length of 0.2 m. The brass connector was 6 mm in diameter and modelled for a thickness of 1 mm.The piezo electric material was attached to a brass piece for easy attachment to the aluminium cylinder. The brass piece was also modelled for better results. The material property of the brass material is as follows

Young's Modulus	E	97 GPa
Poisson's Ratio	ν	0.31
Density	ρ	8490 $\frac{kg}{m^3}$
Radius	r	6 mm
Thickness	t	1mm

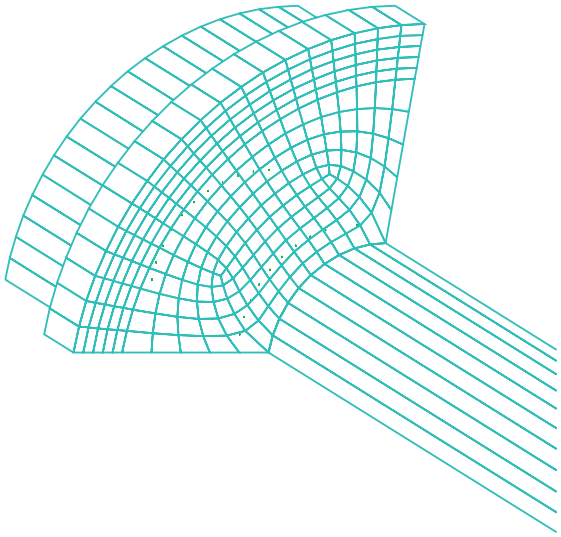

Figure 4.4: 3D View of Type1 Model

4.1.1 Reduction of Electrical Degrees of Freedom

As we can see, the modelled piezo has many electrical degrees of freedom. For our problem where we use the piezo as an actuator, we can reduce the internal electrical degrees of freedom using the technique below and have only the structural degrees of freedom and the known external electrical dof's. It follows directly from [3]. Rewriting the Eqn. 3.53 with u denoting structural degrees of freedom and ϕ denoting the electrical dof's, we have

$$\begin{bmatrix} \mathbf{M}_{\mathrm{ss}} & 0 \\ 0 & 0 \end{bmatrix} \begin{bmatrix} \ddot{\mathbf{u}} \\ \ddot{\phi} \end{bmatrix} \begin{bmatrix} \mathbf{K}_{\mathrm{ss}} & \mathbf{K}_{\mathrm{s}\phi} \\ \mathbf{K}_{\mathrm{s}\phi} & \mathbf{K}_{\phi\phi} \end{bmatrix} \begin{bmatrix} \mathbf{u} \\ \phi \end{bmatrix} = \begin{bmatrix} \mathbf{f} \\ \mathbf{q} \end{bmatrix} \tag{4.1}$$

where $\mathbf{f}$ represents the external forces and $\mathbf{q}$ represents the external electrical charges. The mass matrix M_{ss} contains the initial inertia of the structure only, as quasi-stationarity is assumed for the piezoelectric patches. The structural stiffness matrix is given by the submatrix $\mathbf{K}_{\mathrm{ss}}$ whereas the matrix $\mathbf{K}_{\mathrm{s}\phi}$ couples piezoelectric and structural dynamics. Still now, we have not considered any electrodes for the FE patches. To do so, we partition the electrical potential degrees of freedom ϕ in the piezoelectric patch into degrees of freedom on the potential electrode ϕ_{p}, on the grounded electrode ϕ_{g} and in the interior patch as ϕ_{i} respectively. The latter are not situated in any electrode. Thus the equations of motion in the partitioned form are

given as

$$\begin{bmatrix} \mathbf{M}_{\mathrm{ss}} & 0 & 0 & 0 \\ 0 & 0 & 0 & 0 \\ 0 & 0 & 0 & 0 \\ 0 & 0 & 0 & 0 \end{bmatrix} \begin{bmatrix} \ddot{\mathbf{u}} \\ \ddot{\phi}_{\mathrm{i}} \\ \ddot{\phi}_{\mathrm{p}} \\ \ddot{\phi}_{\mathrm{g}} \end{bmatrix} + \begin{bmatrix} \mathbf{K}_{\mathrm{ss}} & \mathbf{K}_{\mathrm{si}} & \mathbf{K}_{\mathrm{sp}} & \mathbf{K}_{\mathrm{sg}} \\ \mathbf{K}_{\mathrm{si}}^{\mathrm{T}} & \mathbf{K}_{\mathrm{ii}} & \mathbf{K}_{\mathrm{ip}} & \mathbf{K}_{\mathrm{ig}} \\ \mathbf{K}_{\mathrm{ps}}^{\mathrm{T}} & \mathbf{K}_{\mathrm{pi}}^{\mathrm{T}} & \mathbf{K}_{\mathrm{pp}} & \mathbf{K}_{\mathrm{pg}} \\ \mathbf{K}_{\mathrm{gs}}^{\mathrm{T}} & \mathbf{K}_{\mathrm{gi}}^{\mathrm{T}} & \mathbf{K}_{\mathrm{gp}}^{\mathrm{T}} & \mathbf{K}_{\mathrm{gg}} \end{bmatrix} \begin{bmatrix} \mathbf{u} \\ \phi_{\mathrm{i}} \\ \phi_{\mathrm{p}} \\ \phi_{\mathrm{g}} \end{bmatrix} = \begin{bmatrix} \mathbf{f} \\ \mathbf{q}_{\mathrm{i}} \\ \mathbf{q}_{\mathrm{p}} \\ \mathbf{q}_{\mathrm{g}} \end{bmatrix} \tag{4.2}$$

Since the use of the electric potential as a field variable leads to an indeterminacy regarding shifted values, the grounded potential degrees of freedom are set to zero, such that the fourth coloumn in the mass and stiffness matrices may be deleted. Furthermore, the internal potential degrees of freedom ϕ_{i} can be determined by exact static condensation from Eqn. 4.2. It is given as

$$\phi_{\mathrm{i}} = -\mathbf{K}_{\mathrm{ii}}^{-1}\mathbf{K}_{\mathrm{si}}^{\mathrm{T}}\mathbf{u} - \mathbf{K}_{\mathrm{ii}}^{-1}\mathbf{K}_{\mathrm{ip}}\phi_{\mathrm{p}} \tag{4.3}$$

since the internal electrical charges $\mathbf{q}_{\mathrm{i}=0}$ vanish .These two steps finally yield the system of equations

$$\begin{bmatrix} \mathbf{M}_{\mathrm{ss}} & 0 \\ 0 & 0 \end{bmatrix} \begin{bmatrix} \ddot{\mathbf{u}} \\ \ddot{\phi}_{\mathrm{p}} \end{bmatrix} \begin{bmatrix} \mathbf{G}_{\mathrm{ss}} & \mathbf{G}_{\mathrm{sp}} \\ \mathbf{G}_{\mathrm{sp}} & \mathbf{G}_{\mathrm{pp}} \end{bmatrix} \begin{bmatrix} \mathbf{u} \\ \phi_{\mathrm{p}} \end{bmatrix} = \begin{bmatrix} \mathbf{f} \\ \mathbf{q}_{\mathrm{p}} \end{bmatrix} \tag{4.4}$$

with

$$\begin{aligned} \mathbf{G}_{\mathrm{ss}} &= \mathbf{K}_{\mathrm{ss}} - \mathbf{K}_{\mathrm{si}}\mathbf{K}_{\mathrm{ii}}^{-1}\mathbf{K}_{\mathrm{si}}^{\mathrm{T}} \\ \mathbf{G}_{\mathrm{sp}} &= \mathbf{K}_{\mathrm{sp}} - \mathbf{K}_{\mathrm{si}}\mathbf{K}_{\mathrm{ii}}^{-1}\mathbf{K}_{\mathrm{ip}} \\ \mathbf{G}_{\mathrm{pp}} &= \mathbf{K}_{\mathrm{ip}}^{\mathrm{T}} - \mathbf{K}_{\mathrm{si}}\mathbf{K}_{\mathrm{ii}}^{-1}\mathbf{K}_{\mathrm{ip}} \end{aligned} \tag{4.5}$$

With no present electrical charges ,ie $\mathbf{q}_{\mathrm{p}} = 0$ for our problem, we can remove the second line of the Eqn. 4.4 and condense the external potential dependent term to the right hand side as a force term and hence the reduced equation looks as

$$\left[\mathbf{M}_{\mathrm{ss}}\right]\left[\ddot{\mathbf{u}}\right] + \left[\mathbf{G}_{\mathrm{ss}}\right]\left[\mathbf{u}\right] = \left[\mathbf{f} - \mathbf{G}_{\mathrm{sp}}\phi_{\mathrm{p}}\right] \tag{4.6}$$

Thus by using the Eqn. 4.6, we successfully reduce the electrical potential degress of freedom and thus reduce the calculation time. After this, we give an input voltage of 20V and carry on with the simulation and we get the results as below. It is clearly

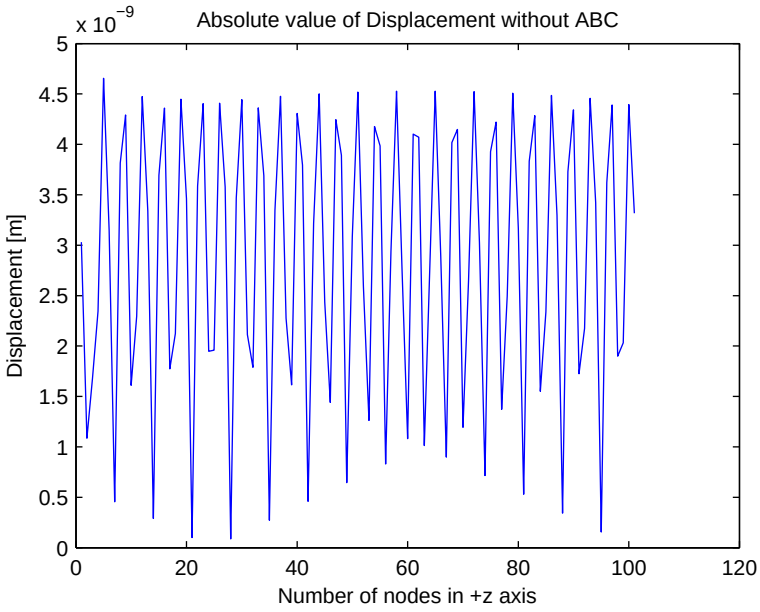

Figure 4.5: Absolute Value of Displacement in z direction for Type1 Model

noted that there is some reflection from end of the rod. We cannot model the rod to be of infinite length and so we restrict the length of the rod that gives rise to reflections. As we can see in Fig. 4.5, a plot of the absolute value of displacement of the travelling wave in z-direction, we see that after the initial excitation due to piezoelectrics, there is no real decrease in the amplitude of the wave, this clearly indicates that the wave has encountered some reflections at the end of the cylinder length. In a real-time scenario, since the length of the wires are very long, no such reflections occur. We cannot also really model the entire length of the wires as this will take too much of a computation time. Hence we need to look out for boundaries that act as a medium to let these incoming waves to get out or in other words absorb these incoming waves.

4.2 Finite Element Modelling of Wave propagation in 3D (Type 2)

The previous type which we modelled could not be used for all the rods together due to the size of the piezo element. This piezo element could not be attached to all the rods to detect the defect. To counter attack this, we thought of another type of setup where we have a piezo plate actuator to be put in place instead of the disc actuator

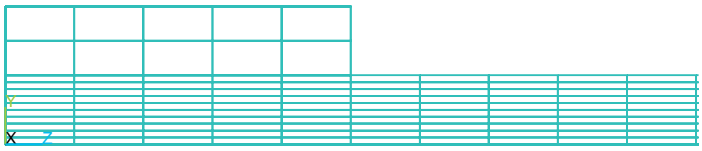

Figure 4.6: Front View of Type2 Model

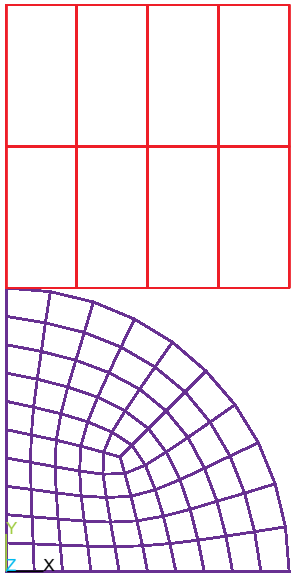

Figure 4.7: Left View of Type2 Model

used in the previous modelling. As we can see from the Fig. 3.8, we can find that the plate actuator can be used to produce the in-plane strain and in turn produce the longitudinal wave in the cylinder. We used the property of symmetry to reduce the computation time. Fig. 4.6 shows the front view of the type 2 model, Fig. 4.7 shows the left side view of the model and Fig. 4.8 shows the three dimensional view of the model as modelled in ANSYS. We can clearly see that the size of piezoelectric actuator is small compared to the cylinder and hence can be placed easily on the wire. There is only a line contact being developed between the cylinder and piezo but that is enough to generate the longitudinal waves.

After reducing the electrical degrees of freedom, we can now plot the absolute value of displacement in the direction of the wave propagation. Fig. 4.9 shows the absolute value of displacement and we can clearly see that there are lot of reflections occuring at the end of the cylinder length. So we require an absorbing boundary condition to model the real-time scenario.

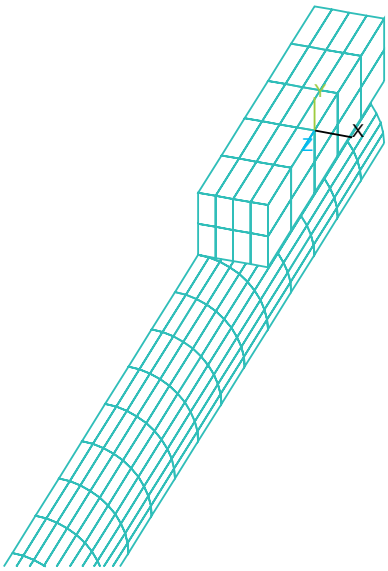

Figure 4.8: 3D View of Type2 Model

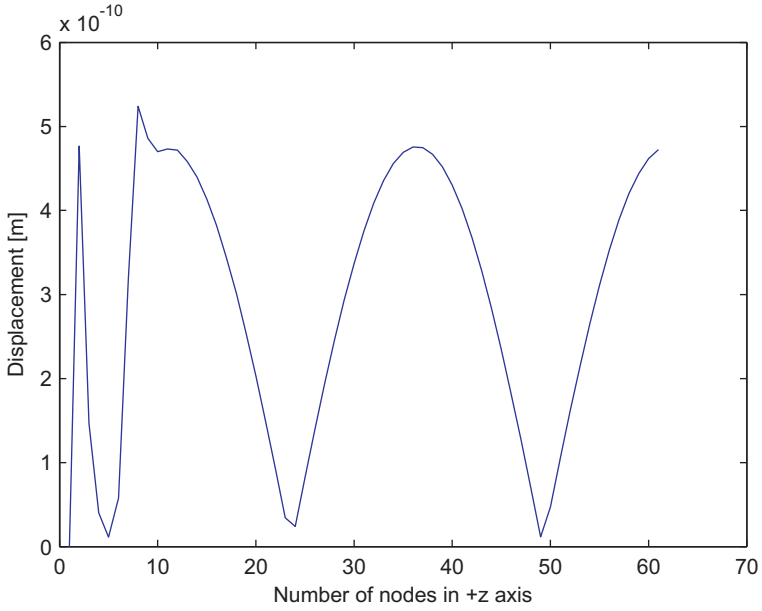

Figure 4.9: Absolute value of Displacement in z direction for Type2 model

5 Absorbing Boundary Conditions

As we have seen in the previous chapter, that we require an absorbing or non-reflecting boundary conditions to reduce the model size and account for proper results as in real life terms. The literature has many models for absorbing boundary conditions.Lysmer and Kuhlmeyer [12] were probably the first ones to propose a non-reflecting bpundary conditions for elastic waves. They introduced damping at the plane of the finite boundary and by choosing appropriate damping constants, they minimize the reflected wave energy.Their method does not prove effective for complex problems [11]. Engquist and Majda [5] found exact non-local boundary conditions and approximated them using local boundary conditions. Givoli and Keller [6] devised a finite artificial circular boundary for a time-harmonic two-dimensional elastodynamics in infinite domains as a global boundary condition. Also the widely cited "Perfectly matched layer" approach by Berenger [4], which uses Finite difference time difference methods are also available for devising a non-reflecting boundary condition. Keys [10] proposes a method by decomposing the wave into incoming and outgoing components. The component that characterizes the outgoing wave fiels is then used to design the absorbing boundary conditions using differential operators. They have a simple physical interpretation, that they absorb the plane waves according to the direction of propagation, thus allowing the direction of propagation as a criteria for designing the absorbing boundary conditions. Higdon [8] developed absorbing boundary conditions in the stratified media for acoustic and elastic waves. He also uses the FTDT method. Liu [11] devices a new method by gradually damping the artificial boundary, where a strip of slowly the amplitude of the wave is decreased to zero thereby resulting in an infinite wave propagation mechanism. This method is proved to be more efficient than the infinite elements method as in the latter case where a sudden change in the damping values form spurious reflections are generated.

The gradually damping method is also discussed only for a two dimensional case. For a three dimensional case, similar to our problem, there are no computationally effective methods in the finite element domain so far used in literature. So we set out to find a new method for developing an absorbing boundary condition at the artificial

boundary so as to make the cylinder a waveguide of infinite length. We start with a one dimensional case to develop our conditions and then extend it over the two dimensional domain to check its possibility of expansion and then apply it to our application.

Another fact that we exploited was that, since our application demands the modelling of propagation of one mode (longitudinal mode in cylinder or symmetrical mode in plate), we decided to restrict the absorbing boundary conditions to just absorb the waves that are produced and not for all the waves that can possibly occur. So the word of caution in using the boundary conditions is that, it is applicable just to one type of waves. But it also has the flexibility to be extended to any type of wave that propagates in the cross-section.

5.1 Fundamentals for Absorbing Boundary Conditions

Any artificial boundary that is designed on the way of a wave propagation, the boundary leads to reflections. These reflections obscure the results and hence the objective stands unachieved. We can derive an absorbing boundary condition, ie, essentially a non-reflecting boundary condition that tries to absorb the waves. This artificaial boundary condition when applied to the boundary makes an impression that the waves pass through the boundary without getting reflected. There is lot of literature available on this subject. RG.Keys [10] proposes a method in which he decomposes the wave equation into incoming and outgoing waves and derive an absorbing boundary condition according to their direction of propagation. This particular decomposition leads to local absorbing boundary conditions obtained directly from the outgoing component of the wave field.

The simple physical interpretation of the boundary conditions of using the direction of wave propagation as a criterion for the design of absorbing boundary conditions makes the problem a much simpler one to solve. Let $\mathbf{a}$ be a vector with unit length such that $\mathbf{a}.\mathbf{a} = 1$, then

$$\left\{\frac{\partial}{\partial x} + \frac{\mathbf{a}}{c}\frac{\partial}{\partial t}\right\}.\left\{\frac{\partial}{\partial x} - \frac{\mathbf{a}}{c}\frac{\partial}{\partial t}\right\}\mathbf{u} = \frac{\partial^2 u}{\partial x^2} + \frac{\mathbf{a}}{c}\frac{\partial^2}{\partial u \partial t} - \frac{\mathbf{a}}{c}\frac{\partial^2}{\partial u \partial t} - \frac{\mathbf{a}.\mathbf{a}}{c^2}\frac{\partial^2 u}{\partial t^2} \tag{5.1}$$

or

$$\left\{\frac{\partial}{\partial x} + \frac{\mathbf{a}}{c}\frac{\partial}{\partial t}\right\}.\left\{\frac{\partial}{\partial x} - \frac{\mathbf{a}}{c}\frac{\partial}{\partial t}\right\}\mathbf{u} = \frac{\partial^2 u}{\partial x^2} - \frac{1}{c^2}\frac{\partial^2 u}{\partial t^2} \tag{5.2}$$

The scalar wave operator in the above equation is decomposed into the inner product of two vector operators. This is arbitary and not unique since the unit vector a was chosen arbitrarily. We consider a plane wave travelling in the direction **a** with a velocity c has the form of displacement as $u(x.\mathbf{a}/ct)$. When the first factor in Eqn. 5.2 is applied to the plane wave, then we have

$$\left\{\frac{\partial}{\partial x}+\frac{\mathbf{a}}{c}\frac{\partial}{\partial t}\right\}u=\mathbf{a}u^{'}-\mathbf{a}u^{'}=0 \tag{5.3}$$

Thus, we have the first vector operator to be used as the identifier for the waves that travel in the direction **a**. Similarly, the second factor gives the waves that travel in the direction $-\mathbf{a}$. Thus the corresponding vector operator can be used in designing the absorbing boundary conditions for the given wave equation. We can also use these operators for designing absorbing boundary conditions in more than one direction. For example, let us assume there are two outgoing plane waves travelling in directions $\mathbf{a}_1$ and $\mathbf{a}_2$, where both are unit vectors, we can see how to derive the absorbing boundary conditions to absorb plane waves travelling in any of these two directions. Let

$$\begin{aligned}&\mathbf{n}_1=\mathbf{a}_1\\&\text{and}\\&\mathbf{n}_2=(\mathbf{a}_1+\mathbf{a}_1)/|\mathbf{a}_1+\mathbf{a}_2|\\&\mathbf{n}_2\text{ is the unit vector in the direction }\mathbf{a}_1+\mathbf{a}_2\end{aligned} \tag{5.4}$$

Let B be the differential operator

$$B(u)=\mathbf{n}_2.\left\{\frac{\partial}{\partial x}+\frac{1}{c}\mathbf{n}_1\frac{\partial}{\partial t}\right\}u \tag{5.5}$$

It is to be noted that $B(u)$ is a scalar function and is therefore compatible with the scalar wave equation. B is referred to as the absorbing boundary operator for the absorption directions $\mathbf{a}_1$ and $\mathbf{a}_2$. The necessary condition for perfect absorption is that the incident wave must satisfy the boundary condition. A reflected wave is created whenever a plane wave strikes the boundary. Thus the total wave field inside the medium is a sum of incident and reflected waves. Thus if the incident wave does not produce any reflections at the boundary it must satisfy the condition $B(u)=0$. If all the absorption directions are oriented in the outgoing direction and if the above

condition is satisfied, then the reflected wave must satisfy the above condition or it must be zero. Since all the absorption directions are outgoing, the reflected wave is an incoming wave, it is impossible for the reflected wave to satisfy the boundary condition. Therefore, no reflected wave is created by the incident plane wave, and the incident plane wave is absorbed without reflection.

Thus we can conclude that if an incident plane wave satisfies the absorbing boundary condition, then it will be absorbed without reflection.

5.2 Implementation of the Absorbing Boundary Conditions

In this section, we will discuss how to implement the above derived basic conditions in one dimension. Then we will test the conditions for one dimension and then extend it to two and three dimensions. We will use the waveguide finite element method discussed before Sec. 2.3.3 to extend the basic equations in three dimensions.

5.2.1 One-dimensional Implementation

Consider the scalar boundary operator given by $B(u)$ to be applied to the direction where the wave propagates. In one dimension, let us consider the direction to be 1. So we have

$$B(u) = \left\{ \frac{\partial}{\partial x} + \frac{1}{c}\frac{\partial}{\partial t} \right\} u = \frac{\partial u}{\partial x} + \frac{1}{c}\frac{\partial u}{\partial t} = 0$$

From the basic relation we know $\sigma = E\epsilon = E\dfrac{\partial u}{\partial x}$

Thus we have $\dfrac{\partial u}{\partial x} = \dfrac{\sigma}{E}$

but $\sigma = \dfrac{F}{A}$

Hence the expression for $B(u)$ becomes $B(u) = F.\dfrac{1}{EA} + \dfrac{1}{c}\dot{u} = 0$ (5.6)

From the above equation, we can find the damping coefficient ,by assuming a simple dash pot model, required to absorb the waves that propagate. Thus from the above equation we can get to

$$F = -\frac{EA}{c}\dot{u} \tag{5.7}$$

Figure 5.1: One dimensional rod model

For a simple dash pot model, the damping coefficient is given by

$$D = \frac{F}{\dot{u}} \tag{5.8}$$

Thus the damping coefficient for wave absorption can be given as

$$D = -\frac{EA}{c}$$
$$\text{but} \quad c = \sqrt{\frac{E}{\rho}}$$
$$\text{substituting we have}$$
$$D = -\sqrt{E\rho}.A \tag{5.9}$$

Now we create a one dimensional model using FEM and check the above derived conditions. If the above derived conditions hold good, and the waves get absorbed by using the derived damping coefficient, then we can conclude that absorbing boundary condition works perfectly in one dimension. So as seen in Fig. 5.1 we have a one dimensional waveguide. We apply the damping to the right most end of the rod and create a wave by exciting the left node of the rod. Then we plot the results of the displacement over the length at two different points in a transient analysis and view the results in Fig. 5.2. This clearly shows that our absorbing boundary condition is working as there are no reflections occurring over time and the entire wave gets absorbed.

5.3 Extension to Two Dimensions - Lamb Waves

We saw that the absorbing boundary conditions work well for a rod. Now we would like to extend the same formulas into the two dimensions so that we can verify the usability of the conditions before further extending it in three dimensions. Another reason for checking the boundary conditions in two dimensions is that we have readily

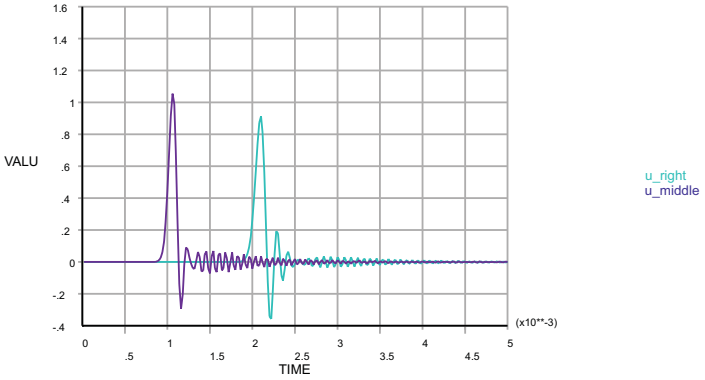

Figure 5.2: Plot of displacements at middle and right end of the rod

the displacement and stress equations and hence the implementation is much quicker and easier.

From Eqn. 2.13 we have the displacement components of the lamb wave given as

$$\begin{aligned} u_1 &= \frac{\partial \phi}{\partial x_1} + \frac{\partial \psi}{\partial x_3} \\ u_2 &= 0 \\ u_3 &= \frac{\partial \phi}{\partial x_3} - \frac{\partial \psi}{\partial x_1} \end{aligned} \tag{5.10}$$

Rewriting the above equation with constants and terms involving only time as we require a differentiation over time to get to the velocity of the wave, we have

$$\begin{aligned} u_1 &= fn(\phi, \psi) \\ u_2 &= 0 \\ u_3 &= fn(\phi, \psi) \end{aligned} \tag{5.11}$$

Similarly from Eqn. 2.11a and Eqn. 2.11b we have

$$\begin{aligned} \phi &= [A_1 \sin(px_3) + A_2 \cos(px_3)] \exp[i(kx_1 - \omega t)] \\ \psi &= [B_1 \sin(qx_3) + B_2 \cos(qx_3)] \exp[i(kx_1 - \omega t)] \end{aligned} \tag{5.12}$$

Again rewriting the above equation just showing the time terms we have

$$\begin{aligned}\phi &= A\exp[i(kx_1 - \omega t)] \\ \phi &= B\exp[i(kx_1 - \omega t)]\end{aligned} \tag{5.13}$$

So we get to the velocity equation of the lamb waves from Eqn. 5.11 and Eqn. 5.13

$$\begin{aligned}\dot{u} &= \frac{\partial u}{\partial t} \\ &= \frac{\partial fn(\phi,\psi)}{\partial t} \\ &= -i * \omega * u\end{aligned} \tag{5.14}$$

Thus we have the $\dot{u}$ term of the damping equation. Now we require the force term to be used in the same equation for the calculation of the damping co-efficient. This can also be easily done by using the stress equations. We assume that we use linear shape functions for the Finite element modelling and hence distribute the stresses onto the nodes. Thus we have the nodal forces given as

$$f = \sigma * \text{element length} \tag{5.15}$$

With the equation for force and velocity found, we can directly compute the damping coefficient for each node. This is given by

$$\mathrm{D} = -\frac{f}{i * \omega * u} \tag{5.16}$$

Thus we get the damping coefficient at each node. We implement the same for a symmetric lamb wave and an anti symmetric lamb wave and the results are shown in the Fig. 2.3 and Fig. 2.4. Thus we prove that the absorbing boundary conditions can be extended to two dimensions. This boundary condition can hence be extended to the third dimension thereby solving our problem of having multiple reflections at the end of the cylinder so that the design of a solution is not possible. In the next section, we will deal as how to implement the boundary conditions in three dimensions and also tackle the challenges involved therein.

5.4 Implementation of the Absorbing Boundary Condition in Three Dimensions

Having established the basic equations for a longitudinal wave in cylinder, it is quite easy to take the same and implement the boundary conditions. But a look through the equations, we find that they are very hard to be solved numerically, leave alone analytically getting to the end. They have a lot of complex functions involved and hence solving those and getting to an absorbing boundary condition is really a tough task. Hence we need to find other ways of getting to the damping coefficient for each node. A close look at the damping equation is given here

$$D = \frac{F}{\dot{u}} \tag{5.17}$$

So we really require the velocity of the travelling wave and the Force that the wave excerts on the node. We use the alternative technique of using the waveguide finite element method [13] to find the displacements and hence the velocities and stresses and hence the force term. As we have discussed in the Sec. 2.3.3, we get to the displacements and forces of the waves that travel through a cross section. The Eqn. 2.66 gives the displacements and forces of the waves travelling in various directions in the cross-section. Based on the direction required for us, we take the corresponding values and compute the damping value using the following equation.

$$D = -\frac{F}{i * \omega * u} \tag{5.18}$$

Thus, we obtain the individual nodal damping factors. We use SDT toolbox in MATLAB for computing the Damping matrix and solving the equations for the Harmonic analysis of wave absorption. Below we present the results for the absorbing boundary conditions implementation. Having done the implementation of the absorbing boundary conditions, we can now decide upon selecting the right frequency for the piezo actuator so that we can measure the wave propagation taking place in the material.

6 Design of Piezoelectric Transducers

With the newly developed absorbing boundary conditions in our hand, we are now ready to go directly to our problem of designing the piezoelectric transducers. This chapter will discuss in detail how to apply the absorbing boundary conditions to the cylinders and how to analyse the results from the simulations. We will be mainly concentrating on designing the operating frequency of the piezo as the dimensions of the piezo availble to us is already defined. We can, after designing the frequency of operation and verifying it with measurement, use this method to change the dimensions of the actuator and verify whether it can suit our needs.

6.1 Piezoelectric Transducer Type I

We will now design the piezoelectric transducers having a circular cross-section and classified as disc transducers. For the process of designing the displacements produced by such an actuator, we apply the non-reflecting boundary conditions for the model described in section 4.1. As shown there, we construct the model using ANSYS® and export the Mass and stiffness matrices along with the node, elements and material properties into MATLAB® with the help of Structural Dynamics Toolbox (SDT) available in MATLAB®. As discussed before, for this application of checking the structural health, we will use the longitudinal waves as they propagate faster in the cylinders and also propagate long distances. So we need to apply the boundary conditions for a propagating longitudinal wave in the right end of the model as we can see that the peizoelectric transducers are in the left end of the cylinders. We also can use the symmetric property of the longitudinal wave in modelling the wave. This helps for us to reduce the calculation time and get better results as we can see below. The Fig. 6.1 was modelled for finding the propagating modes occuring in this cross-section. As discussed earlier, only a longitudinal wave can propagate in this cross-section. The boundary condition is directly applied from this cross-section and applied to the cylinder ends. Since the displacement from the longitudinal waves is an exponential function, when viewing in a frequency domain, the negative phase angle change over

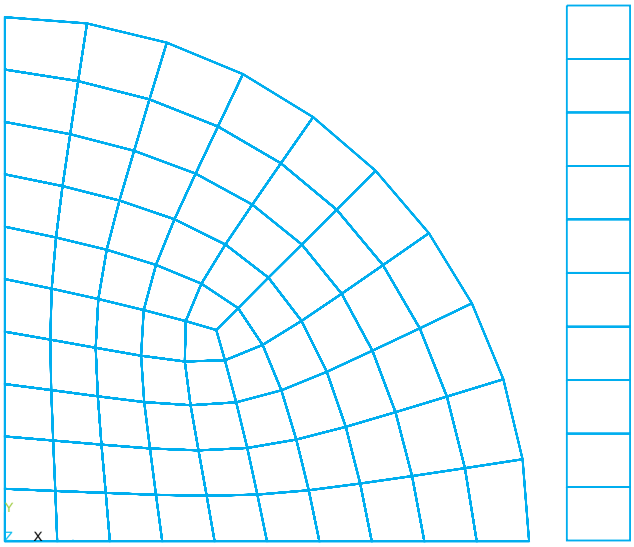

Figure 6.1: Finite Element Model of section of waveguide

the length of propagation will show a wave propagation in the structure. This will be the first step to be checked while applying the absorbing boundary conditions. A plot of the phase angle of the travelling wave over the length of propagation will give a clear idea as whether there is a wave propagation occuring. Fig. 6.2 shows the phase angle of the travelling wave at 50kHz and we clearly see that there is a continuous negative phase angle throughout the wave changing with distance. This clearly proves that the wave is travelling in the cylinder. This plot is plotted at 50kHz frequency with a 20V input to the piezoelectric transducer. Comparing the same to the phase angle of the propagating wave without using absorbing boundary conditions shown in Fig. 6.3, we can clearly say that due to the reflections, the phase angle of the travelling wave is almost same over change in length signifying no change in the displacement. Thus we find that the absorbing boundary conditions are working in the real-time scenario. Now we have determined that the wave is travelling in the cylinder, we must plot the absolute value of the displacement of the wave in the wave propagation direction. Fig. 6.4 shows the plot of absolute value of displacement for 3D model type 1. This graph is plotted at x=0.001 m , y= 0.001 m and z= 0 to 0.2 m. It is plotted at a frequency of 50 kHz, and has 100 nodes along the z-axis. As we can see the displacements are in the expected range of 10 nanometers. This now proves that the way of modelling is working. So now we can see how the piezoelectric transducer changes the displacement values.

We create a frequency vector from 50Khz to 500kHz and check for the maximum

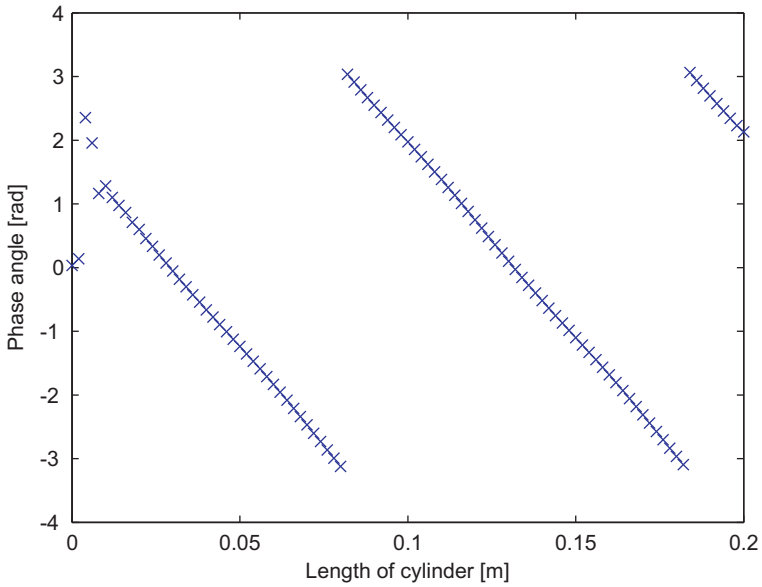

Figure 6.2: Phase angle of Travelling wave with ABC's

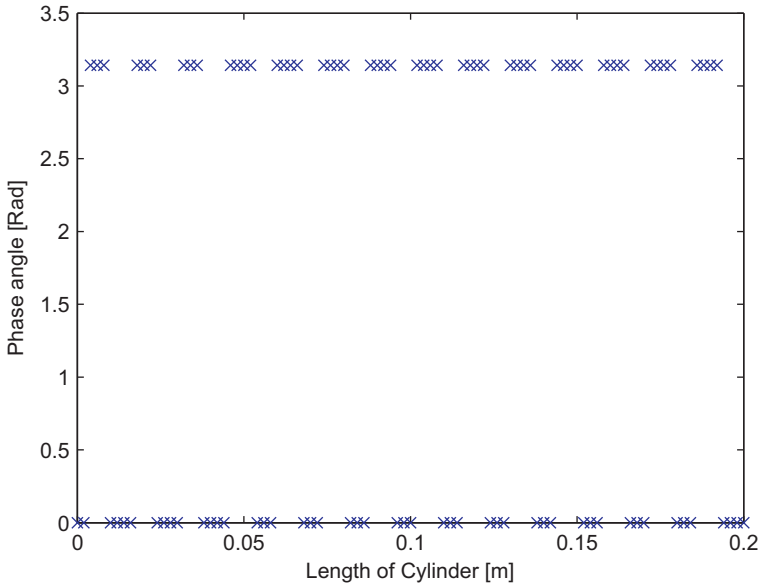

Figure 6.3: Phase angle of Travelling wave without ABC's

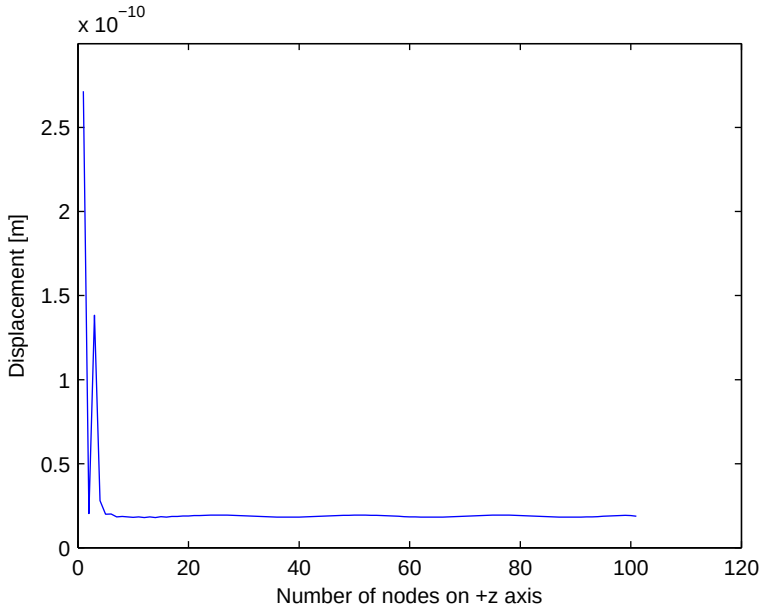

Figure 6.4: Absolute value of displacement for 3D model type1 using ABC's

value of displacement in the same line as described above. We plot the absolute value of displacement and absolute value of displacement in +z direction (u_3) value of displacement. We clearly see that the piezoelectric transducer produces the maximum value of displacement at a frequency 370 kHz. So, when we use a piezoelectric transducer of type 1, we need to use a frequency of 370 kHz, so that we can have maximum displacement in the cylinder. Thus the cracks can be detected clearly.

6.2 Piezoelectric Transducer Type II

After having found suitable frequncy of operation for the circular piezoelectric transducer, we can now find a similar operation frequency for the type 2 model. We first check the phase angle and find that there is a wave propagation occuring. We now plot the absolute value of the displacement along the direction of wave propagation. To check our boundary conditions, we use a new technique where we compare the displacement plot by changing the lengths of the cylinder. The behaviour of the curve is expected to be similar even when changng the length of the cylinder as the absorbing boundary conditions should absorb all the waves coming in its direction. Fig. 6.6 shows the absolute value of displacement over frequency for type2 model. We clearly see the displacement is in the range of nanometers and also the change in

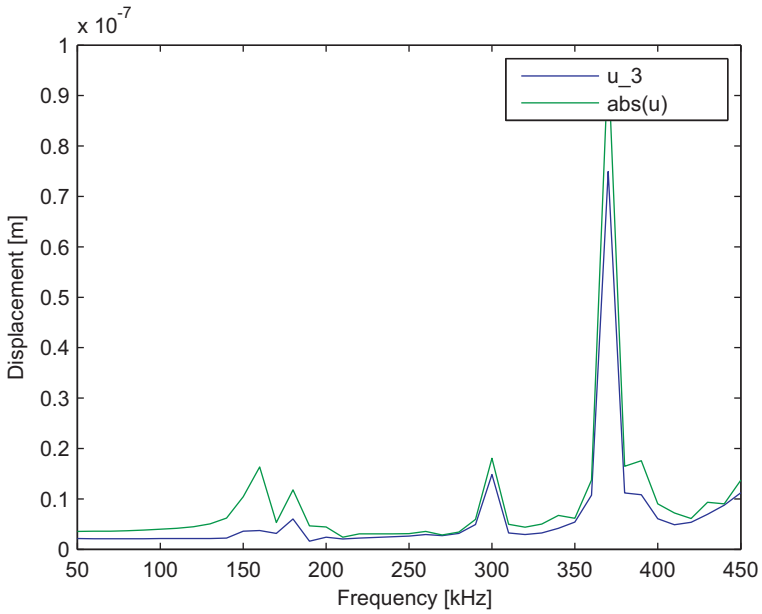

Figure 6.5: Absolute displacement over Frequency for Type1 Model

geometry does not considerably change the values of the solution. Thus we are quite sure that the absorbing boundary conditions are working perfectly.

Now we create a frequency vector from 50kHz to 500kHz and find the maximum value of displacement occurs at a frequency of 240 kHz. Another proof of the modelling is that, we can clearly see that eventhough there is a change in the length of the cylinder, the maximum displacement always occurs at a frequency of 240 kHz.

Thus we can say that whenever the block type of piezoelectric transducer is used, it is best to use it in the frequency range of 240kHz and we can identify the cracks easily. Another important point to note in mind is that all these values hold good only for the geometry of the pieozoelectric transducer we have specified in the previous chapters. This geometry was not optimized as this was the standard piezo material as supplied for use. There is also a possibility to alter this geometry and find the best possible geometry. As we can clearly see from the results, the type 1 piezoelectric transducer is performing better than the type 2 piezoelectric transducer.

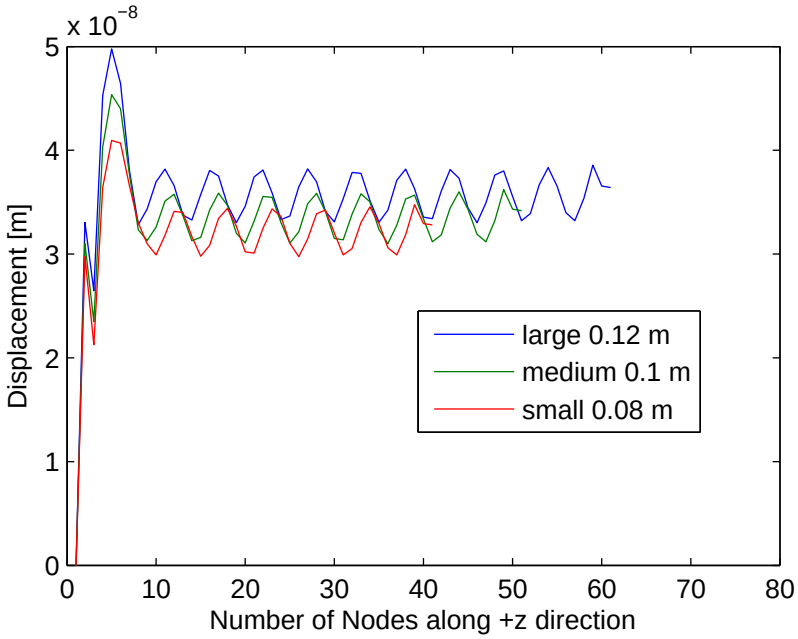

Figure 6.6: Absolute displacement over Frequency for Type2 Model

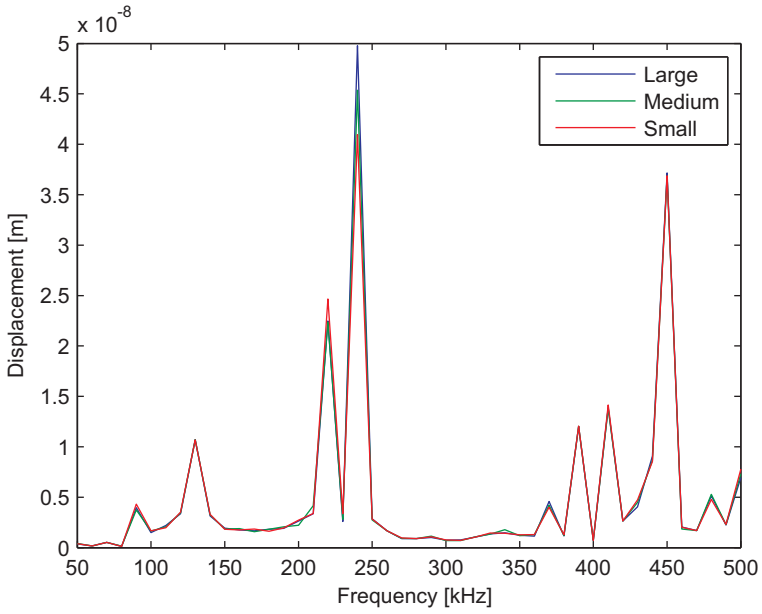

Figure 6.7: Absolute displacement over Frequency for Type2 Model

7 Conclusion

A brief introduction to the mathematics behind wave propagation was explained. The long distant travelling waves in plate like structures namely the lamb waves and the elastic waves in the cylinders was introduced. Using the waveguide based finite element method, the propagation of lamb waves in plate like structures and elastic waves in cylindrical structures was modelled and plotted. This gave a clear idea as how wave propagation is occurring in these type of structures.

The piezoelectric material, its material properties, the coupled electro-mechanical formulations were discussed and then the piezoelectric transducer was successfully modelled using the finite element method. Various geometries of the piezoelectric actuator was also considered and they were used in modelling the generation of longitudinal waves in cylinders. They resulted in reflections at the artificial boundaries of the cylinder and hence the results were not correct.

To tackle this problem, a new type of absorbing boundary condition was developed that made use of the waveguide based finite element method, this greatly reduced the computation time and also made the results meaningful. This generalized method was tested in one- dimension, extended to two- dimension and then was applied to three- dimensional problem. This condition proved really effective in designing the piezoelectric transducer.

When a circular piezoelectric transducer is used, it is attached to the end of the cylinder and its operation frequency could be set at 370 kHz when the displacement occuring in the structure is maximum. Similarly when a piezoelectric transducer similar to a block is used, the structure and the piezoelectric transducer have only a line contact. In this case, the frequency of operation of piezoelectric transducer can be set at 240 kHz. Also, the block model produced a much higher displacement level compared to the circular piezoelectric transducer.

With the absorbing boundary conditions now being designed, it would be nice to compare them with physical measurements and ascertain the credibility of the conditions and their equivalence to the physical behaviour. At the time of writing, various methods are under investigation to measure the displacements in the cylindrical rods.

Again it is to be noted that since the cylindrical rod cannot be physically tested in lab conditions for infinite distances, we might make use of packet signals that are sent in discrete packets and measurements are made on the system before the reflection from the end of the rod affects the measurement. From a structural maintenance point of view, a measurement procedure is to be developed to measure the displacements. This measurement procedure can be utilized in determining the worthiness of the absorbing boundary condition.

Another interesting direction would be to model the contact between the cylindrical rods. There is a friction coupled energy based analysis of contacts between rods, but with the help of absorbing boundary conditions, we can make a finite element based model for contact analysis. Since the contact geometry is quite complex, the simple step would be to model two rods with one acting as an active rod and the other a passive rod and to examine the wave propagation in the contact area. When we use the piezoelectric transducers of type 2 as discussed in the previous chapters, we might be using both the rods as active rods. Since the piezoelectric transducers can be attached only to the outer surface of the multiple wire system, it would be exciting to model contacts and find the displacements in the innermost wires. Also it would be interesting to model the reflections in the innermost wire due to the cracks present in them. The use of absorbing boundary conditions becomes inevitable when such complicated modelling is done.

Bibliography

[1] Achenbach, J. D.: *Wave Propagation in Elastic Solids*. first. Elsevier, 1999

[2] A.Grohmann, Boris: *Lecture Notes on Smart Piezo Structures, Uni Stuttgart*. June 2009

[3] Becker, J. ; Fein, O. ; Maess, M. ; Gaul, L.: Finite element-based analysis of shunted piezoelectric structures for vibration damping. In: *Computers and Structures* 84 (2006), Nr. 31-32, S. 2340–2350

[4] Berenger, J.P.: A perfectly matched layer for the absorption of electromagnetic waves. In: *Journal of computational physics* 114 (1994), Nr. 2, S. 185–200

[5] Engquist, B. ; Majda, A.: Radiation boundary conditions for acoustic and elastic wave calculations. In: *Comm.Pure.App.Math 32* (1979), S. 313–357

[6] Givoli, D.: Non-reflecting boundary conditions. In: *Journal of Computational Physics* 94 (1991), Nr. 1, S. 1–29

[7] Haag, T. ; Beadle, B.M. ; Sprenger, H. ; Gaul, L.: Wave-based defect detection and interwire friction modeling for overhead transmission lines. In: *Archive of Applied Mechanics* 79 (2009), Nr. 6, S. 517–528

[8] Higdon, R.L.: Absorbing boundary conditions for acoustic and elastic waves in stratified media. In: *Journal of Computational Physics* 101 (1992), Nr. 2, S. 386–418

[9] Karl.F.Graff: *Wave Motion in Elastic Solids*. First. Dover, 1991

[10] Keys, RG: Absorbing boundary conditions for acoustic media. In: *Geophysics* 50 (1985), S. 892

[11] Liu, GR ; Jerry, Q.: A non-reflecting boundary for analyzing wave propagation using the finite element method. In: *Finite Elements in Analysis and Design* 39 (2003), Nr. 5-6, S. 403–417

[12] Lysmer, J. ; Kuhlemeyer, RL: Finite dynamic model for infinite media. In: *J.Eng.Mech.Div.ASCE 95* (1969), S. 859–877

[13] Mace, B.R. ; Duhamel, D. ; Brennan, M.J. ; Hinke, L.: Finite element prediction of wave motion in structural waveguides. In: *The Journal of the Acoustical Society of America* 117 (2005), S. 2835

[14] Meitzler, A.H.: Mode coupling occurring in the propagation of elastic pulses in wires. In: *The Journal of the Acoustical Society of America* 33 (1961), S. 435

[15] Nienwenhui, JH ; Neumann Jr, JJ ; Greve, DW ; Oppenheim, IJ: Generation and detection of guided waves using PZT wafer transducers. In: *IEEE Transactions on Ultrasonics, Ferroelectrics and Frequency Control* 52 (2005), Nr. 11, S. 2103–2111

[16] Rizzo, P. ; Scalea, F. Lanza di: Wave propagation in multi-wire strands by wavelet-based laser ultrasound. In: *Experimental Mechanics* 44 (2004), Nr. 4, S. 407–415

[17] Su, Z. ; Ye, L.: *Identification of Damage Using Lamb Waves: From Fundamentals to Applications*. Springer Verlag, 2009

[18] Su, Z. ; Ye, L. ; Lu, Y.: Guided Lamb waves for identification of damage in composite structures: a review. In: *Journal of Sound and Vibration* 295 (2006), Nr. 3-5, S. 753–780